A High-Resolution Earthquake Catalog Reveals Coupled Fault Interactions and Multiple Controls on Seismicity Migration in an Intraplate Earthquake Swarm

Ratna Bhagat[1,2], Pathikrit Bhattacharya[1,2], K M Sreejith[3], Harsha S. Bhat[4], Vineet K. Gahalaut[5,6]

[1]National Institute of Science Education and Research, Jatni, Odisha 752050, India
[2]Homi Bhabha National Institute, Training School Complex, Anushakti Nagar, Mumbai 400094, India
[3]Geosciences Division, Space Applications Centre, Indian Space Research Organisation, Ahmedabad, 380015, India
[4]Laboratoire de Geologie, École Normale Supérieure, CNRS-UMR 8538, PSL Research University, 75005 Paris, France
[5]Wadia Institute of Himalayan Geology, Dehradun, Uttarakhand, 248001, India
[6]CSIR-National Geophysical Research Institute, Hyderabad-500007, India

Key Points:

- New machine-learned and relocated catalog reveals reveals two interacting fault zones within the 2019–2020 Palghar intraplate swarm.
- Seismicity migrated as both diffusive and faster-than-diffusive propagating fronts, indicating multiple triggering processes.
- Fault interactions, elastic stress transfer, and possible fluid-assisted deformation jointly govern swarm evolution.

Corresponding author: Pathikrit Bhattacharya, `pathikritb@niser.ac.in`

Abstract

Earthquake swarms in intraplate regions provide a unique opportunity to study fault responses to transient perturbations under low background strain rates. We investigate the 2019-2020 Palghar swarm in western India using data from two local seismic networks to construct a machine-learning-enhanced catalog comprising ∼50,000 events. High-resolution event relocations and moment tensor solutions reveal reactivation of two shallow normal faults with associated damage zones extending to ∼8 km depth. Seismicity initiates on the western fault, migrates to the eastern fault, and expands into the damage zones, indicating triggering through fault interactions. Broadly diffusive seismicity migration interspersed with persistent seismicity clusters and faster-than-diffusive migration transients suggests the involvement of both crustal fluids and aseismic slip. Together, these observations show that the evolution of intraplate earthquake swarms may be governed by seismic and aseismic elastic stress transfer coupled with fluid-driven processes, demonstrating how high-resolution earthquake catalogs help disentangle the processes controlling swarm evolution.

Plain-language summary:

Earthquake swarms represent clusters of seismicity that occur over days to years without a single large mainshock. In stable continental regions, where earthquakes do not originate due to tectonic forcing, these swarms provide valuable clues about what other processes within the earth's crust causes faults to become active. We investigated the 2019–2020 Palghar earthquake swarm in western India using recordings from two local seismic networks and a machine learning method that detected nearly 50,000 earthquakes. We found that the earthquakes occurred on two shallow, preexisting faults. The activity began on one fault, later migrated to the other, and eventually spread into the area between them. The observed migration of these earthquakes indicates that underground fluids and slow, silent movement along faults might have acted together to control the swarm's evolution. These findings improve our understanding of how earthquake swarms develop in stable continental regions and provide new insights into the processes that control seismic activity far away from plate boundaries.

1 Introduction

Earthquake swarms are clusters of seismicity that occur close together in space and time without a clearly identifiable initiating event (Mogi, 1962; Hill, 1977; Vidale & Shearer, 2006). Swarm activity commonly exhibits complex spatiotemporal migration of seismicity, reflecting the combined influence of multiple physical processes rather than a single triggering mechanism (Hainzl, 2004; Roland & McGuire, 2009; Ruhl et al., 2016; Danré et al., 2022; Fischer et al., 2023; Danré et al., 2024). Characterizing these migration patterns, therefore, provides an important means of distinguishing among the processes responsible for swarm evolution. For example, slow, diffusive migration is commonly interpreted as reflecting fluid-mediated processes wherein the seismicity front is phenomenologically linked to the migration of a pore-pressure diffusion front (Shapiro & Dinske, 2009; Fischer & Hainzl, 2021; Danré et al., 2022). In contrast, faster-than-diffusive migration may reflect elastic stress transfer arising from a wide range of processes, including poroelastic responses to fluid flow within deformable porous media, the rapid propagation of aseismic slip fronts, and stress redistribution through elastic interactions within actively deforming fault networks (Hill, 1977; Rao et al., 1991; Hainzl, 2004; Goebel et al., 2017; Bhattacharya & Viesca, 2019; Hatch et al., 2020; Danré et al., 2024; Almakari et al., 2026). Determining the processes that govern swarm evolution is important for understanding earthquake triggering, the physical controls on the spatiotemporal evolution of earthquake clusters, and the partitioning of strain-energy release across event sizes (Vidale & Shearer, 2006; Roland & McGuire, 2009; Hatch et al., 2020; Ross et al., 2020; Danré et al., 2024). Intraplate swarms are particularly valuable in this context because they provide a rare window into fault responses to transient stress perturbations under low long-term strain rates, where transient perturbations to fault stability can exceed the secular strain accumulation in amplitude (Hill, 1977; Ellsworth, 2013).

Many intraplate swarms are triggered by transient stress or strength perturbations and are often associated with pre-existing zones of crustal weakness (Rastogi et al., 1997; Stevenson et al., 2006; Srinagesh et al., 2020). Within the stable continental crust of India, several such swarms have been reported, but most are short-lived and poorly monitored, limiting insights into their driving mechanisms (Srivastava & Dube, 1996; Sateesh et al., 2019; Wadhawan et al., 2021). Of these, the Palghar swarm is an exception in that it continued for over two years and produced, as we show later, many tens of thousands of events and was well monitored by multiple seismic networks deployed by government agencies (Srinagesh et al., 2020; Gahalaut et al., 2022; Sharma et al., 2023). Most of the seismic activity occurred within the granitoid basement of the Deccan Volcanic Province within a relatively simple fault system that enables clear interpretation of fault–seismicity relations (Sharma et al., 2020; Pavankumar et al., 2020; Nath et al., 2021). Previous studies, based on smaller, local seismic networks and multiple geophysical observations, have suggested the presence of fluids within the fractured upper crust in the Palghar swarm region (Pavankumar et al., 2020; Nath et al., 2021; Subhadra & Shekar, 2024; Kanaujia et al., 2025). However, substantial discrepancies in hypocentral locations between the seismicity catalogs derived from two major local networks limit our ability to resolve the swarm's migration patterns and, consequently, to identify the physical processes controlling its initiation and evolution (Sharma et al., 2020; Srinagesh et al., 2020). As a result, the relative roles of pore-pressure diffusion, aseismic slip (if any), and fault-seismicity interactions, as well as the possible source of the fluids, all remain poorly constrained.

Resolving the contribution of these processes requires a dense catalog with accurate earthquake locations, as precise hypocenters and source-property estimates are essential for diagnosing swarm driving mechanisms. To achieve this, we merge waveform data from two local seismic networks to construct a region-specific velocity model and a unified, high-resolution earthquake catalog for the Palghar swarm. We use a machine-learning-based detection workflow to substantially densify the earthquake catalog and refine earthquake locations using relocations based on waveform cross-correlation derived differential travel times. The resulting catalog resolves the three-dimensional geometry and spatiotemporal evolution of the Palghar swarm, revealing two closely spaced fault zones and deformation within an intervening damage zone. We show that seismicity migrated between the two faults through a combination of diffusion-like expansion and transient episodes of rapid propagation, indicating the combined influence of elastic fault interactions, crustal fluids, and transient aseismic slip. These observations demonstrate how fault interactions and transient deformation govern the evolution of intraplate earthquake swarms and provide new insight into earthquake triggering under low background strain-rate regimes.

2 Geological setting, data and methods

The Palghar region lies on the western margin of the Deccan Volcanic Province (DVP), where ∼1.5 km thick basalt flows overlie Archaean–Proterozoic basement rocks and are dissected by inherited rift-related structures, including the Panvel flexure, the West Coast Fault, and several N–S trending basement-rooted lineaments (Auden, 1949; Courtillot et al., 1986, 2003; Chandrasekharam, 1985; Gunnell & Fleitout, 1998; Sheth, 1998; Nath et al., 2021; Sharma et al., 2020, 2023). These inherited structures have hosted diverse modes of seismicity in the past, from the 1993 Latur earthquake and reservoir-triggered seismicity at Koyna to recurrent earthquake swarms (Rao et al., 1991; Srivastava & Dube, 1996; Raju et al., 2000; Hainzl et al., 2014; Sateesh et al., 2019; Wadhawan et al., 2021).

Among these swarms, the Palghar sequence stands out for its unusually long duration (over two years), high event count (tens of thousands of earthquakes), and dense instrumental coverage, providing a rare opportunity to constrain—if not the triggering mechanisms—at least the processes governing its evolution (Sharma et al., 2020, 2023; Gahalaut et al., 2022). Previous studies have linked the Palghar swarm to both meteoric-water infiltration and deeper crustal fluids (Pavankumar et al., 2020; Srinagesh et al., 2020; Sharma et al., 2020; Nath et al., 2021; Gahalaut et al., 2022; Kanaujia et al., 2025). Its exceptional duration and productivity provide a unique opportunity to investigate the processes governing earthquake clustering and fault reactivation within the Deccan Volcanic Province, with broader implications for intraplate seismicity worldwide.

2.1 Seismic Data

This study uses waveform data from 11 broadband stations operated independently by the National Geophysical Research Institute (NGRI) and the National Center for Seismology (NCS) following the onset of the Palghar swarm, providing dense coverage over an area of approximately 30 km × 30 km (Sharma et al., 2020; Gahalaut et al., 2022) (SI Figure S1). We merge the independently compiled NGRI and NCS catalogs by matching events within 0.5 s of their origin times, yielding a unified dataset with an improved mean azimuthal gap (∼80°) compared with the individual NCS (∼158°) and NGRI (∼94°) networks (SI Figure S5). Earthquakes recorded by at least ten stations are used to derive a one-dimensional velocity model (Section 2.2), which is subsequently used for earthquake detection, absolute locations, relative relocations, and moment tensor inversions. All remaining catalog construction steps rely on automated detection and relative location procedures. Station coordinates and elevations are listed in SI Table 1.

2.2 One-Dimensional Velocity Modeling

Previous studies adopted different velocity models for the NGRI and NCS datasets, resulting in substantial discrepancies in earthquake depths (6-7 km Sharma et al. (2020) to 4-16 km Srinagesh et al. (2020)). To obtain a consistent velocity model for the merged dataset, we applied joint hypocenter determination (JHD) using `VELEST` (Kissling et al., 1995). The inversion used 2,514 well-recorded human-picked earthquakes observed at ten or more stations, yielding 25,097 P- and 24,361 S-wave arrivals. A constant V_p/V_s ratio of 1.71, estimated from the linear relationship between P- and S-wave arrival times (SI Figure S2), was assumed throughout the inversions.

The one-dimensional model of Srinagesh et al. (2020) was used as the initial reference. To assess model stability and minimize dependence on the starting model, we generated ensembles of randomly perturbed velocity models by varying layer velocities (± 0.7 km s^{-1}) and interface depths (± 2 km) within prescribed ranges. Three successive inversion stages (see SI materials for details) comprising 210 perturbed models in total converged to an ensemble of solutions at the end of the third stage (Figure 1). The mean velocity model from this final ensemble was adopted for all subsequent earthquake detection, location, and moment tensor analyses. Station corrections estimated during the inversion account for near-surface heterogeneity and were applied in subsequent relocations.

2.3 ML-based earthquake detection and relocation

Further earthquake detection and hypocentral determination were performed using a multi-stage, fully automated workflow designed to construct a dense and internally consistent earthquake catalog for the Palghar swarm. The workflow combines network-based detection using the BPMF (**B**ack **P**rojection and **M**atched **F**iltering) framework (Beaucé et al., 2024), probabilistic absolute location, and high-precision relative relocation, without reliance on manual phase picking for catalog construction.

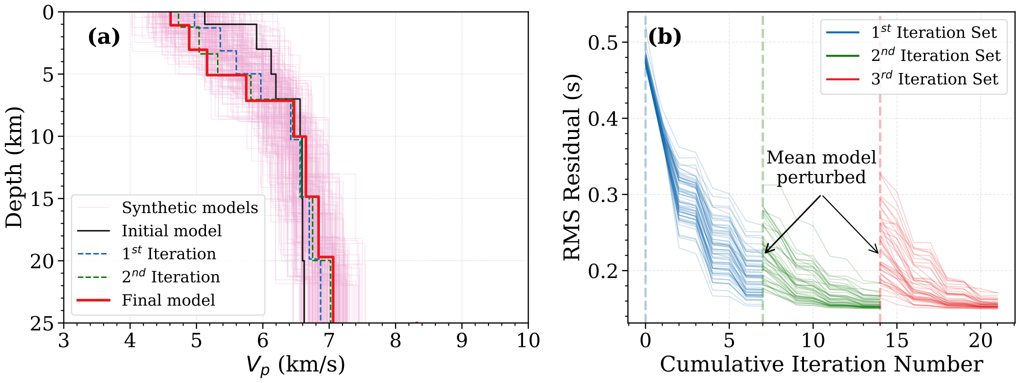

Figure 1. Joint hypocenter–velocity inversion results for the Palghar swarm region using `VELEST`. (a) Velocity inversion results after three inversion stages. The initial velocity model of Srinagesh et al. (2020) is shown in black. At each stage, an ensemble of velocity models was generated by randomly perturbing the final mean model from the previous stage by ±0.7 km s^{-1} in layer velocity and ±2 km in interface depth to assess inversion stability. The resulting ensemble of final velocity models across all 3 stages is shown in pink, and the mean at the end of the stage 3 (thick red line) was adopted in this study. Blue and green dashed lines denote the mean velocity models obtained after the first and second inversion stages, respectively. (b) Evolution of RMS travel-time residuals during the inversion. Vertical dashed lines indicate the boundaries between the three inversion stages.

Continuous three-component waveform data were first processed using the deep-learning phase picker PhaseNet (Zhu & Beroza, 2019) to estimate P- and S-wave arrival probabilities. These probabilities were used in the back projection workflow developed by (Beaucé et al., 2024), which coherently stacked phase-consistent arrival probabilities using theoretical moveout corrections computed from the one-dimensional velocity model (Section 2.2). Events exceeding a predefined beam-power threshold (SI Figure S6) yielded an initial catalog of 57,826 earthquakes.

These initial grid-based hypocenters obtained from the back projection procedure were subsequently refined using the probabilistic location algorithm `NonLinLoc` (Lomax et al., 2000). Retaining only events recorded at six or more stations produced 20,638 earthquakes with median horizontal and depth uncertainties of 0.5 km and 1.5 km, respectively (Figure S7). High-precision relative locations were then obtained using `GrowClust` (Trugman & Shearer, 2017) and waveform cross-correlation of 5–10 Hz filtered seismograms. Event pairs sharing at least six observations with cross-correlation coefficients ≥ 0.8 were retained, resulting in a final catalog of 16,008 earthquakes. In comparison, the manually picked catalog contains only 5,765 well-recorded events.

The relocated seismicity delineates two narrow, subparallel north–south–striking fault strands confined to depths of 2–6 km (Figure 2). Bootstrap analysis indicates median relative location uncertainties of 250 m horizontally and 320 m vertically (SI Figure S7), sufficient to robustly resolve fault geometry and swarm evolution.

2.4 Moment Tensor Inversions

To constrain the faulting style of the larger earthquakes within the swarm, we performed moment tensor (MT) inversions for 37 events ($M_l \geq 3.0$) using `MTTime` (Ichinose

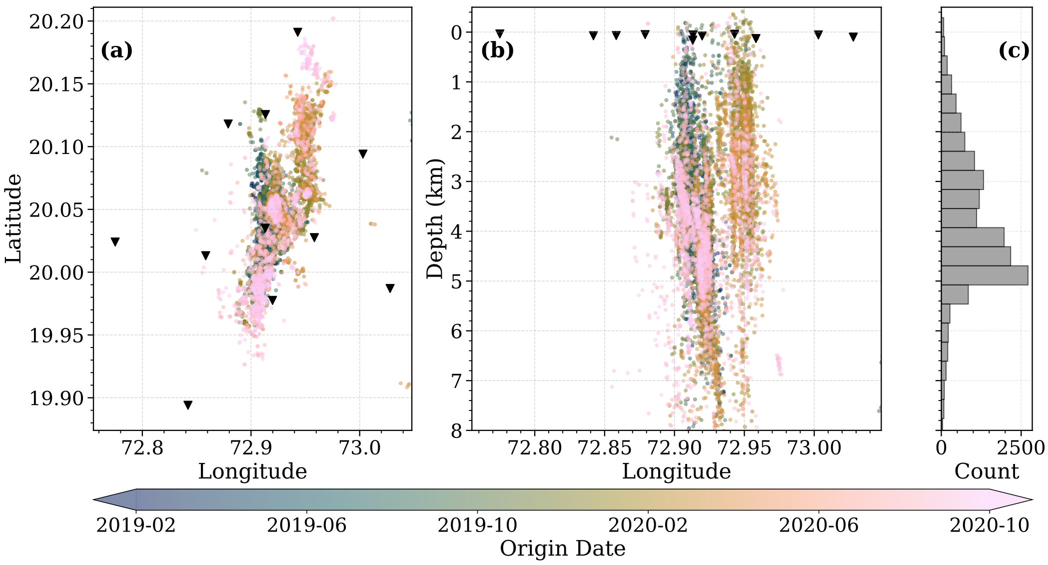

Figure 2. Spatial distribution of the `GrowClust`-relocated Palghar earthquake swarm. (a) Map view, and (b) longitude–depth cross-section of relocated seismicity color-coded by origin time, illustrating the spatiotemporal evolution of the swarm. Black inverted triangles denote seismic station locations projected onto the section. (c) Histogram of hypocenter depths showing that seismicity is predominantly concentrated between about 2 and 6 km. The flood basalt is expected to be not more than 1.5 km thick in this region. Therefore, the seismicity is almost entirely concentrated within the granitoid basement.

et al., 2014) (see SI materials for details, Text S3). Green's functions were computed with the CPS package (Herrmann, 2013) using the one-dimensional velocity model derived in this study. Relative locations from `GrowClust` were used where available, and `NonLinLoc` hypocenters were adopted for the remaining nine events. Waveforms were filtered between 0.05 and 1 Hz, and all selected solutions achieved variance reductions exceeding 50% (SI Figure S10; SI Table 2).

The MT solutions indicate predominantly normal faulting with minor strike-slip components (Figures 3 and S10). Fault strikes closely follow the north–south trends of the linear structures outlined by the relocated seismicity, whereas dip angles cluster around $\sim 30^\circ$ and $\sim 60^\circ$, consistent with conjugate normal faults (SI Figure S9). The rake angles are likewise consistent with dominantly extensional slip. Together, these observations indicate reactivation of pre-existing extensional fault structures and justify interpreting the two relocated seismicity clusters as outlining two subparallel normal faults which we refer to as the western and eastern faults in the subsequent analysis.

3 Results

The high-resolution ML-enhanced relocated earthquake catalogs developed in this study provide substantially improved constraints on the spatiotemporal evolution of the Palghar swarm compared to the human-picked catalog that earlier studies have mostly relied upon (Sharma et al., 2020, 2023; Srinagesh et al., 2020) (SI Figure S11). During the first ~200 days, seismicity remains confined to a cluster around the western fault before a sudden appearance of seismicity that clusters around the eastern fault (Figures 4a and b). We choose to label the seismicity as western, eastern and off-fault clusters depending on whether the events are within a band of ±1 km around each of the visually

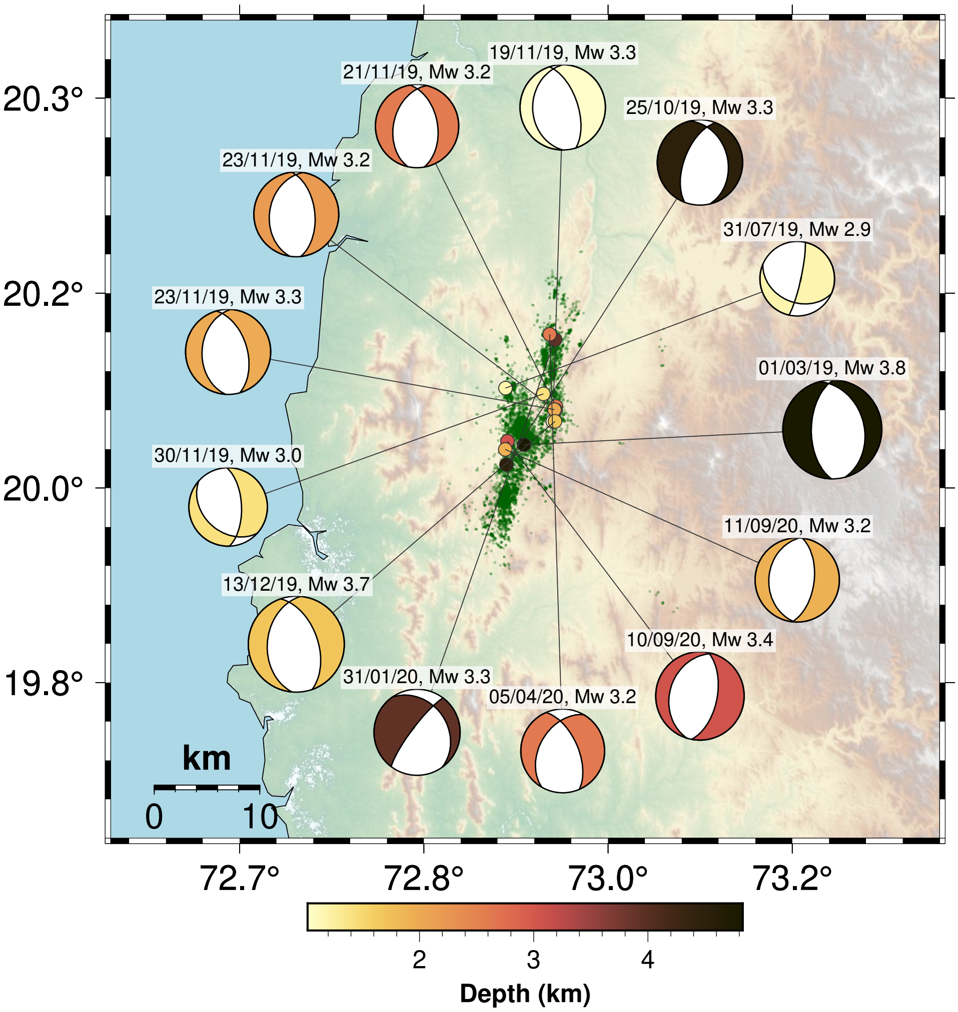

Figure 3. Moment tensor solutions for earthquakes with $M_l \geq 3.0$ and variance reduction exceeding 50%. Beachball size scales with magnitude, and colors indicate event depth. Green dots show relocated hypocenters from the full catalog (all events relocated by `GrowClust` plus 9 supplemented from `NonLinLoc`). Only the double-couple component is displayed; full deviatoric solutions are shown in the SI figure S8.

interpreted fault structures. The ‘off-fault’ earthquakes between the two faults are predominantly activated only after seismicity begins to cluster around both faults likely reflecting ruptures activated by stress perturbations generated by simultaneous activation of slip on both faults.

We analyze the spatiotemporal evolution of the Palghar earthquake swarm using an epicentral-distance vs. time representation of the relocated events, where the former is measured relative to the first recorded event from the machine-learned catalog (Origin time: 01/02/2019 00:01:53, latitude: 20.04°, longitude: 72.91°, depth: 2.4 km) (Figure 4). The seismicity migration reveals a broad expansion of earthquake activity over time (Figure 4d). The overall envelope is consistent with diffusive growth, with most events bounded by diffusivities of ∼0.005–0.3 m^2 s^{-1}. Superimposed on this long-term expansion are distinct propagating fronts that define the leading edge of the swarm. These fronts are most pronounced during activation of the eastern fault between ∼260 and 460 days,

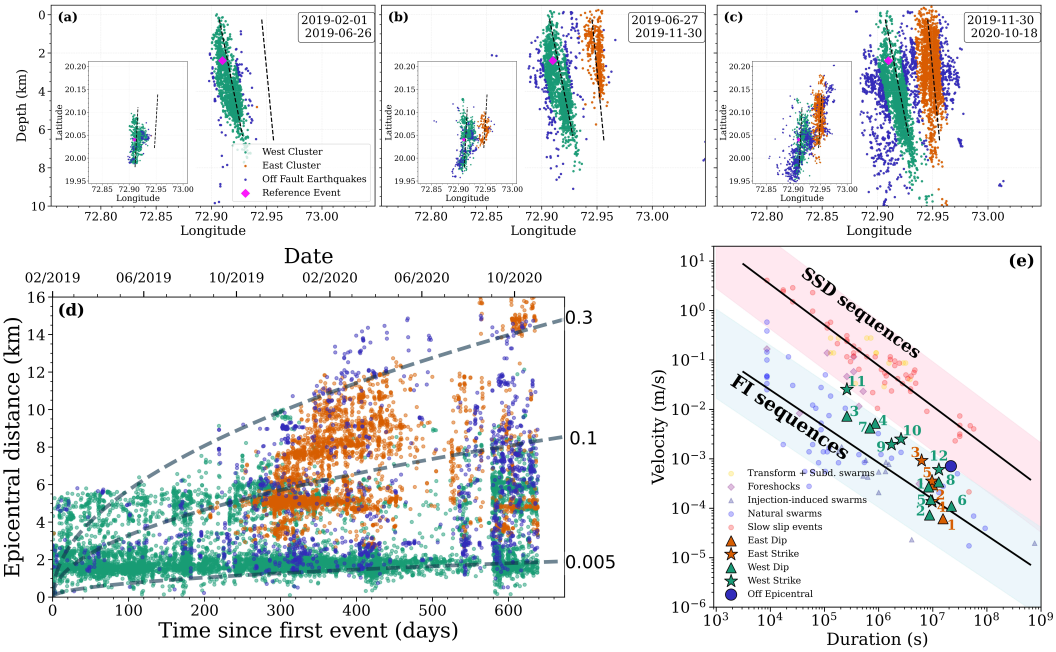

Figure 4. Spatiotemporal evolution and migration characteristics of the Palghar swarm. (a–c) Relocated earthquakes projected onto longitude–depth sections for the western (green), eastern (orange), and off-fault (blue) clusters. Insets show map views. (d) Epicentral distance versus time with reference diffusion fronts (0.005, 0.1, and 0.3 m^2/s). (e) Migration velocity versus duration for representative migration episodes in the Palghar swarm plotted within the fluid-induced (FI) and slow-slip–driven (SSD) migration regimes proposed by Danré et al. (2024). Stars and triangles denote along-strike and along-dip migration episodes, respectively (for details, see SI Figures S13, S14 and S15). Green, orange, and blue symbols represent the western fault, eastern fault, and off-fault migration episodes respectively.

when earthquakes progressively migrate to larger epicentral distances. In contrast, the western fault remains active throughout most of the sequence, with repeated migration episodes nucleating from a persistent source region near 1.5 km epicentral distance.

The inferred ‘fault’ structures shown in Figures 4a-c clearly show that the epicentral distance migration is nearly insensitive to any along-dip migration given the steeply dipping normal ‘faults’ inferred from the seismicity clustering. Given this, we differentiate the along-strike and dip migrations of the western and eastern clusters to better constrain the rupturing process (SI Figures S13 and S14). The along-dip and along-strike distance-time evolution of seismicity along the western fault reveals strongly episodic migration behavior. The persistent seismicity band becomes more conspicuous and appears both strike- and dip-limited, while multiple seismicity fronts propagate, along-strike and dip, both away and towards this seismicity band over time. The along-strike and along-dip migration envelopes reveal multiple episodes of outward and back-propagating seismicity fronts on the western fault (SI Figures S13a, c). Migration rates and durations for representative episodes are compared with the velocity-duration classification of Danré et al. (2024) in Figure 4e.

In contrast, the eastern fault exhibits a very different seismicity clustering, with much of the early migration occurring prominently northwards along strike, accompanied by slower back-propagating fronts both along strike and dip (SI Figure S14a and c). There is a non-persistent seismicity band visible only along strike, but this mostly disappears after about 450 days of seismicity. As for the western cluster, we again estimate the migration rates for some of the visually distinct migration periods and report these within the Danré et al. (2024) classification scheme for reference.

The off-fault seismicity exhibits migration patterns similar to those of the eastern cluster, with nearly identical epicentral migration rates between ∼260 and ∼360 days (SI Figure S15). During this interval, much of the off-fault seismicity represents northward migration adjacent to the eastern fault. These observations are robust to a narrower (±500 m) definition of the fault zones (SI Figure S15). Later in the sequence (∼ 480 to ∼640 days), off-fault seismicity mirrors the southward and updip migration observed along the western fault (SI Figure S16).

4 Discussion

The new high-resolution earthquake catalog reveals a substantially more complex evolution of the Palghar swarm than previously recognized (Srinagesh et al., 2020; Sharma et al., 2020, 2023; Nath et al., 2021). Rather than occurring on a single fault zone, the swarm initiated on one of two closely spaced fault segments before migrating to the second one and, finally, progressively expanded into the surrounding fault damage zone. The relocated seismicity further reveals persistent fault-localized activity on the western fault, together with transient propagating fronts, indicating that the observed swarm evolution cannot be explained by a single triggering mechanism. These newly resolved spatiotemporal patterns provide important constraints on the physical processes governing earthquake swarms.

The overall migration of seismicity is consistent with a broad diffusive envelope, with apparent hydraulic diffusivities ranging from ∼0.005 to ∼0.3 $m^2\ s^{-1}$, comparable to values reported for fluid-driven swarms elsewhere (Goebel et al., 2017; Cabrera et al., 2021). Superimposed on this long-term expansion are transient propagation fronts that migrate substantially faster than expected from diffusion alone. In the migration velocity–duration space of Danré et al. (2024), most of the observed migrations fall within the fluid-diffusion regime, whereas a smaller population approaches the transition toward the slow-slip regime identified by Danré et al. (2024) (episodes 3 from the eastern and 3, 4, 7 and 11 from the western clusters in Figure 4e). Although none of the observed faster migration episodes lie unequivocally within the slow-slip regime, the coexistence of distinct migration populations suggests that multiple transient processes contributed to swarm evolution. Additionally, direct comparison with the transitional boundaries proposed by Danré et al. (2024) should be interpreted with caution because their slow-slip–driven migration dataset is derived primarily from epicentral migration in plate-boundary settings, whereas our migration rates are based on along-strike and along-dip propagation within an intraplate fault system.

The inference that multiple processes contributed to swarm evolution is also consistent with contrasting migration styles on the western and eastern fault systems. The western fault hosts a persistent, spatially confined seismicity band from which seismicity repeatedly expands and contracts along strike and dip (SI Figure S13a, c), whereas the eastern fault is dominated by a transient along-strike migration episode that contains several of the $M_l > 3.0$ earthquakes and lacks a comparable persistent seismicity cluster (SI Figure S14a, c). Additionally, off-fault seismicity between and adjacent to the faults closely mirrors on-fault migration. Following activation of the eastern fault, both on-fault and off-fault seismicity propagated northward at comparable rates during the 260–460 day interval (see SI Figure S15). Similar correspondence is observed west of the western fault, where off-fault seismicity tracks the along-strike and up-dip migration of the main cluster (SI Figure S16). This coordinated spatiotemporal evolution is difficult to reconcile with diffusive processes alone and instead suggests that transient aseismic deformation and elastic stress transfer operated together with diffusive (possibly fluid-assisted) processes.

The Palghar swarm is strongly confined to depths shallower than ∼6 km (Figure 2c). Such a sharp lower bound may reflect structural termination of the active fault network, a permeability barrier restricting deeper fluid migration, or a rheological transition at depth. Because the swarm is hosted within the granitoid basement of the Deccan Volcanic Province, where extensive dyke-related fault networks are expected (Courtillot et al., 1986; Rubin & Pollard, 1988; Rubin, 1992), structural termination at only ∼6 km appears unlikely (Rai & Saha, 2025). Likewise, a rheological transition from velocity-weakening to velocity-strengthening friction is difficult to reconcile with the shallow cut-off, regional geothermal gradients (M. L. Gupta & Gaur, 1984; Roy & Rao, 2000; C. Scholz, 1998; C. H. Scholz, 2019), and evidence for deeper crustal low-velocity zones in nearby swarm regions (Rai & Saha, 2025). Given that the persistent seismicity band within the western cluster is also not much wider than ∼1 km along both strike and dip, we favor a model in which the persistent seismicity band on the western fault marks a localized fault-valve system connected to a deeper fluid source, with downdip fluid migration limited by permeability barriers or pore-pressure gradients. Such a persistent fluid reservoir may also have provided the initial perturbation that triggered the swarm.

Previous studies have attributed the Palghar swarm and similar earthquake swarms in the Deccan Volcanic Province to monsoon-driven recharge (Hainzl et al., 2014; H. K. Gupta, 2018; Sharma et al., 2020; Nath et al., 2021; Gahalaut et al., 2022; Sharma et al., 2023). In contrast, the densified catalog does not reveal a systematic relationship between rainfall and seismicity during the early, most productive phase of the sequence, although one increase in seismicity during the later stages follows the end of the monsoon season (SI Figure S18). While these observations do not exclude a contribution from meteoric recharge, they provide little evidence that rainfall alone controlled swarm initiation. Instead, our results favor a deeper fluid source whose interaction with fault geometry and elastic stress transfer governed the evolution of the Palghar swarm.

5 Conclusion

Previous studies of the Palghar earthquake swarm relied primarily on human-picked, independently developed catalogs from the NGRI and NCS seismic networks which lacked the event density and location precision necessary to fully resolve the physical processes governing the swarm evolution. In this study, we combined waveform data from both networks and constructed an macine-learning-enhanced high-resolution earthquake catalog to better illuminate the mechanisms controlling the swarm sequence. The refined relocations reveal two closely spaced structurally-controlled seismicity clusters between depths of approximately 2-8 km, together with distributed off-fault earthquakes between them. The spatiotemporal evolution of the sequence exhibits strongly contrasting migration behaviors between the two fault systems which we interpret as diagnostic of at least two different physical processes driving the initiation and continued evolution of the swarm.

The overall swarm evolution remains broadly diffusive, suggestive of fluid-driven migration, whereas several rapid migration episodes approach the transitional regime commonly associated with transient aseismic slip. At the same time, the delayed activation of the eastern cluster and the subsequent emergence of off-fault seismicity provide strong evidence for elastic stress transfer both between the two principal fault systems and among earthquakes occurring within the surrounding fault damage zone. While transient aseismic slip may have contributed to at least some of the rapid migration episodes, the Palghar sequence more broadly illustrates how long-lived earthquake swarms in stable continental interiors can emerge from coupled interactions among (possible) fluid migration, transient aseismic deformation, and stress transfer within structurally complex inherited fault networks. More generally, our results demonstrate that high-resolution earthquake catalogs, combined with detailed fault geometry and spatiotemporal migration analyses, can distinguish among these interacting processes and provide new constraints on the physical mechanisms governing intraplate earthquake swarms.

References

Almakari, M., Kheirdast, N., Villafuerte, C., Thomas, M., Dubernet, P., Cheng, J., … Bhat, H. (2026). Fault volume digital twin to reproduce the full slip spectrum, scaling, and statistical laws. *Journal of Geophysical Research: Solid Earth*, *131*(5), e2025JB032915.

Auden, J. (1949). Dykes in western india-a discussion on their relationships with the deccan traps. *Trans. Nat. Inst. Sci. India*, *3*, 123–157.

Beaucé, E., Frank, W. B., Seydoux, L., Poli, P., Groebner, N., van der Hilst, R. D., & Campillo, M. (2024). Bpmf: A backprojection and matched-filtering workflow for automated earthquake detection and location. *Seismological Research Letters*, *95*(2A), 1030–1042.

Bhattacharya, P., & Viesca, R. C. (2019). Fluid-induced aseismic fault slip outpaces pore-fluid migration. *Science*, *364*(6439), 464–468.

Cabrera, L., Poli, P., & Frank, W. B. (2021). Tracking the spatio-temporal evolution of foreshocks preceding the mw 6.3 2009 l'aquila earthquake 2. *interaction*, *14*, 15.

Chandrasekharam, D. (1985). Structure and evolution of the western continental margin of india deduced from gravity, seismic, geomagnetic and geochronological studies. *Physics of the Earth and Planetary interiors*, *41*(2-3), 186–198.

Courtillot, V., Besse, J., Vandamme, D., Montigny, R., Jaeger, J.-J., & Cappetta, H. (1986). Deccan flood basalts at the cretaceous/tertiary boundary? *Earth and Planetary Science Letters*, *80*(3-4), 361–374.

Courtillot, V., Davaille, A., Besse, J., & Stock, J. (2003). Three distinct types of hotspots in the earth's mantle. *Earth and Planetary Science Letters*, *205*(3-4), 295–308.

Danré, P., De Barros, L., Cappa, F., & Ampuero, J.-P. (2022). Prevalence of aseismic slip linking fluid injection to natural and anthropogenic seismic swarms. *Journal of Geophysical Research: Solid Earth*, *127*(12), e2022JB025571.

Danré, P., De Barros, L., Cappa, F., & Passarelli, L. (2024). Parallel dynamics of slow slips and fluid-induced seismic swarms. *Nature Communications*, *15*(1), 8943.

Ellsworth, W. L. (2013). Injection-induced earthquakes. *science*, *341*(6142), 1225942.

Fischer, T., & Hainzl, S. (2021). The growth of earthquake clusters. *Frontiers in Earth Science*, *9*, 638336.

Fischer, T., Hainzl, S., & Vlček, J. (2023). Fast migration episodes within earthquake swarms. *Geophysical Journal International*, *235*(1), 312–325.

Gahalaut, K., Gahalaut, V., Naresh, B., Shekar, M., Sunilkumar, T., & Srinagesh, D. (2022). Long duration non-volcanic and non-tectonic palghar earthquake swarm in the stable continental region of india—role of seasonal rainfall and earthquake cascading. *Journal of Seismology*, *26*(3), 545–554.

Goebel, T., Weingarten, M., Chen, X., Haffener, J., & Brodsky, E. (2017). The 2016 mw5. 1 fairview, oklahoma earthquakes: Evidence for long-range poroelastic triggering at¿ 40 km from fluid disposal wells. *Earth and Planetary Science Letters*, *472*, 50–61.

Gunnell, Y., & Fleitout, L. (1998). Shoulder uplift of the western ghats passive margin, india: a denudational model. *Earth Surface Processes and Landforms: The Journal of the British Geomorphological Group*, *23*(5), 391–404.

Gupta, H. K. (2018). Reservoir triggered seismicity (rts) at koyna, india, over the past 50 yrs. *Bulletin of the Seismological Society of America*, *108*(5B), 2907–2918.

Gupta, M. L., & Gaur, V. K. (1984). Surface heat flow and probable evolution of deccan volcanism. *Tectonophysics*, *105*(1–4), 309–318.

Hainzl, S. (2004). Seismicity patterns of earthquake swarms due to fluid intrusion and stress triggering. *Geophysical Journal International*, *159*(3), 1090–1096.

Hainzl, S., Aggarwal, S., Khan, P., & Rastogi, B. (2014). Monsoon-induced earthquake activity in talala, gujarat, india. *Geophysical Journal International*, *200*(1), 627–637.

Hatch, R. L., Abercrombie, R. E., Ruhl, C. J., & Smith, K. D. (2020). Evidence of aseismic and fluid-driven processes in a small complex seismic swarm near virginia city, nevada. *Geophysical Research Letters*, *47*(4), e2019GL085477.

Herrmann, R. B. (2013). Computer programs in seismology: An evolving tool for instruction and research. *Seismological Research Letters*, *84*(6), 1081–1088.

Hill, D. P. (1977). A model for earthquake swarms. *Journal of Geophysical Research*, *82*(8), 1347–1352.

Ichinose, G., Roman-Nieves, J., & Kraft, G. (2014). Moment tensor inversion toolkit (mtinv) documentation, manual and tutorial. *Seismol. Res. Lett.*(2), 37–57.

Kanaujia, J., Kumar, M. R., Vengala, P. K., & Shekar, M. (2025). Indication of fluid-driven seismicity in the palghar region, india, from local earthquake tomography. *Bulletin of the Seismological Society of America*, *115*(2), 489–504.

Kissling, E., Kradolfer, U., & Maurer, H. (1995). Program velest user's guide-short introduction. *Institute of Geophysics, ETH Zurich*, *22*.

Lomax, A., Virieux, J., Volant, P., & Berge-Thierry, C. (2000). Probabilistic earthquake location in 3d and layered models: Introduction of a metropolis-gibbs method and comparison with linear locations. In *Advances in seismic event location* (pp. 101–134). Springer.

Mogi, K. (1962). Magnitude-frequency relation for elastic shocks accompanying fractures of various materials and some related problems in earthquakes. *Bull. Earthq. Res. Inst., Univ. Tokyo*, *40*, 831–853.

Nath, B., Singh, R. P., Gahalaut, V. K., & Singh, A. P. (2021). Dynamic relationship study between the observed seismicity and spatiotemporal pattern of lineament changes in palghar, north maharashtra (india). *Remote Sensing*, *14*(1), 135.

Pavankumar, G., Chakravarthi, N., Demudu Babu, M., & Manglik, A. (2020). Magnetotelluric study of an intraplate seismic zone in the palghar region of the deccan volcanic province, india. *Journal of Earth System Science*, *129*(1), 133.

Rai, S. S., & Saha, G. (2025). Deccan volcanism and related seismic unrest in the koyna–warna region, india. *Seismological Research Letters*, *96*(3), 1645–1653.

Raju, P. S., Srinivasan, A., Raghavan, R., & Kousalya, M. (2000). Micro-tremor activity in jubilee hills area of hyderabad, andhra pradesh. *Geological Society of India*, 443–445.

Rao, D., Jambusaria, B., Srivastava, S., Srivastava, N., Hamid, A., Desai, B., & Srivastava, H. (1991). Earthquake swarm activity in south gujarat. *Mausam*, *42*(1), 89–98.

Rastogi, B., Mandal, P., & Kumar, N. (1997). Seismicity around dhamni dam, maharashtra, india. *pure and applied geophysics*, *150*(3), 493–509.

Roland, E., & McGuire, J. J. (2009). Earthquake swarms on transform faults. *Geophysical Journal International*, *178*(3), 1677–1690.

Ross, Z. E., Cochran, E. S., Trugman, D. T., & Smith, J. D. (2020). 3d fault architecture controls the dynamism of earthquake swarms. *Science*, *368*(6497), 1357–1361.

Roy, S., & Rao, R. (2000). Heat flow in the indian shield. *Journal of Geophysical Research: Solid Earth*, *105*(B11), 25587–25604.

Rubin, A. M. (1992). Dike-induced faulting and graben subsidence in volcanic rift zones. *Journal of Geophysical Research: Solid Earth*, *97*(B2), 1839–1858.

Rubin, A. M., & Pollard, D. D. (1988). Dike-induced faulting in rift zones of iceland and afar. *Geology*, *16*(5), 413–417.

Ruhl, C., Abercrombie, R., Smith, K., & Zaliapin, I. (2016). Complex spatiotemporal evolution of the 2008 mw 4.9 mogul earthquake swarm (reno, nevada): Interplay of fluid and faulting. *Journal of Geophysical Research: Solid Earth*, *121*(11), 8196–8216.

Sateesh, A., Mahesh, P., Singh, A., Kumar, S., Chopra, S., & Kumar, M. R. (2019). Are earthquake swarms in south gujarat, northwestern deccan volcanic province of india monsoon induced? *Environmental Earth Sciences*, *78*(13), 381.

Scholz, C. (1998). Earthquakes and friction laws. *Nature*, *391*, 37–42. doi: 10.1038/34097

Scholz, C. H. (2019). *The mechanics of earthquakes and faulting*. Cambridge university press.

Shapiro, S. A., & Dinske, C. (2009). Fluid-induced seismicity: Pressure diffusion and hydraulic fracturing. *Geophysical Prospecting*, *57*(2), 301–310.

Sharma, V., Kumar, D., Sharma, B., & Chingtham, P. (2023). Characteristics of earthquake swarm activity observed in the palghar region of indian peninsula from january 2019 to october 2020. *Quaternary Science Advances*, *12*, 100099.

Sharma, V., Wadhawan, M., Rana, N., Sreejith, K., Agrawal, R., Kamra, C., … Gahalaut, V. K. (2020). A long duration non-volcanic earthquake sequence in the stable continental region of india: The palghar swarm. *Tectonophysics*, *779*, 228376.

Sheth, H. (1998). A reappraisal of the coastal panvel flexure, deccan traps, as a listric-fault-controlled reverse drag structure. *Tectonophysics*, *294*(1-2), 143–149.

Srinagesh, D., Singh, D. K., Vikas, G., Naresh, B., Roy, S., Murthy, Y., … others (2020). An appraisal of recent earthquake activity in palghar region, maharashtra, india. *Curr Sci*, *118*, 1592–1598.

Srivastava, H., & Dube, R. (1996). Comparison of precursory and non-precursory swarm activity in peninsular india. *Tectonophysics*, *265*(3-4), 327–339.

Stevenson, D., Gangopadhyay, A., & Talwani, P. (2006). Booming plutons: Source of microearthquakes in south carolina. *Geophysical Research Letters*, *33*(3).

Subhadra, N., & Shekar, M. (2024). The attenuation mechanism of high-frequency seismic waves in the palghar swarm earthquake source area in western india. *Journal of Asian Earth Sciences*, *276*, 106306.

Trugman, D. T., & Shearer, P. M. (2017). Growclust: A hierarchical clustering algorithm for relative earthquake relocation, with application to the spanish springs and sheldon, nevada, earthquake sequences. *Seismological Research Letters*, *88*(2A), 379–391.

Vidale, J. E., & Shearer, P. M. (2006). A survey of 71 earthquake bursts across southern california: Exploring the role of pore fluid pressure fluctuations and aseismic slip as drivers. *Journal of Geophysical Research: Solid Earth*, *111*(B5).

Wadhawan, M., Rana, N., Gahalaut, V., Singh, M., Singh, K., Suresh, G., … others (2021). Monsoonal rainfall induced shallow earthquake swarm in the amravati district of the central india. *Journal of Earth System Science*, *130*(1), 29.

Zhu, W., & Beroza, G. C. (2019). Phasenet: a deep-neural-network-based seismic arrival-time picking method. *Geophysical Journal International*, *216*(1), 261–273.

Supporting Information

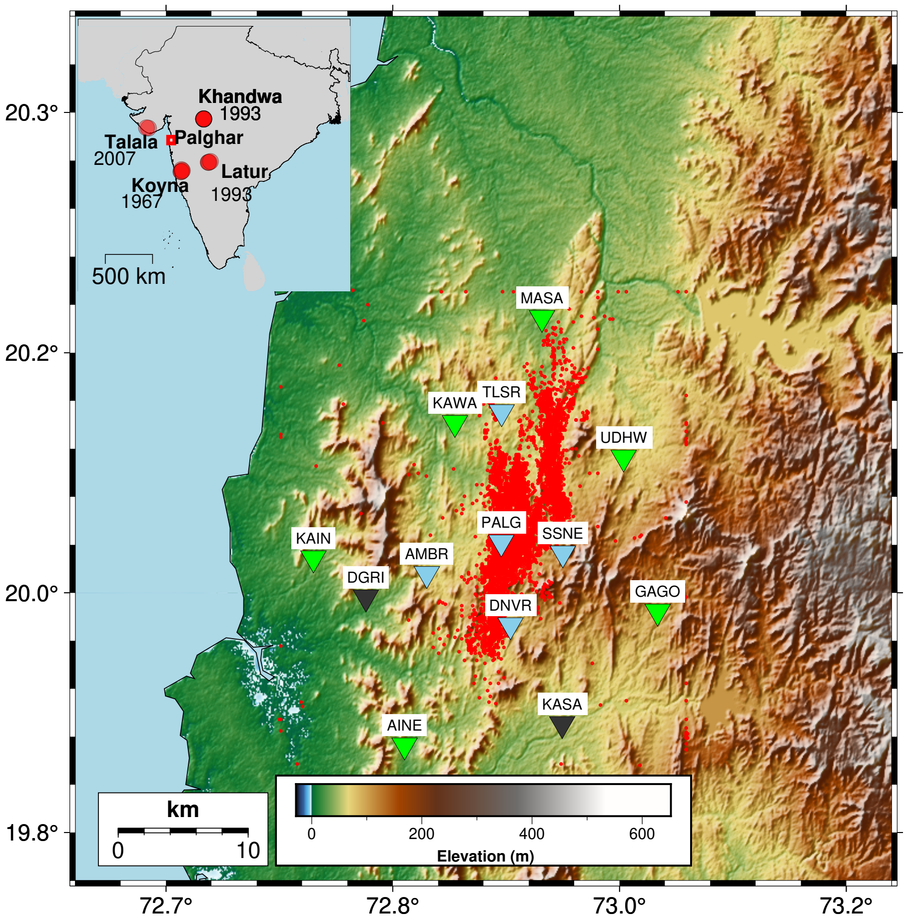

Figure S1. Map of the Palghar region showing the distribution of the seismic stations (triangles) used in this study. Green triangles denote stations operated by NGRI, while sky-blue triangles denote those operated by NCS. Note that the KASA and DGRI stations were later relocated to TLSR and DNVR, respectively, which were also managed by NCS. Red dots represent earthquake epicenters derived from machine learning–based detections and located using NonLinLoc. The inset map of India highlights the Palghar region (red box) and marks other major intraplate earthquakes and swarm occurrences across the Indian peninsular region.

Text S1. Velocity Model Constraints and Robustness Tests

To evaluate the robustness of the final 1-D velocity model derived for the Palghar swarm, we examine the stability of the inversion results, the sensitivity of the recovered velocity structure, and the consistency of the adopted V_p/V_s ratio.

S1.1 Estimation of the V_p/V_s Ratio

The V_p/V_s ratio used in the velocity inversion was independently estimated from the manually picked P- and S-wave arrival times of the earthquakes used for velocity modeling. Figure S2 shows the relationship between the differential S- and P-wave travel (Δt_S

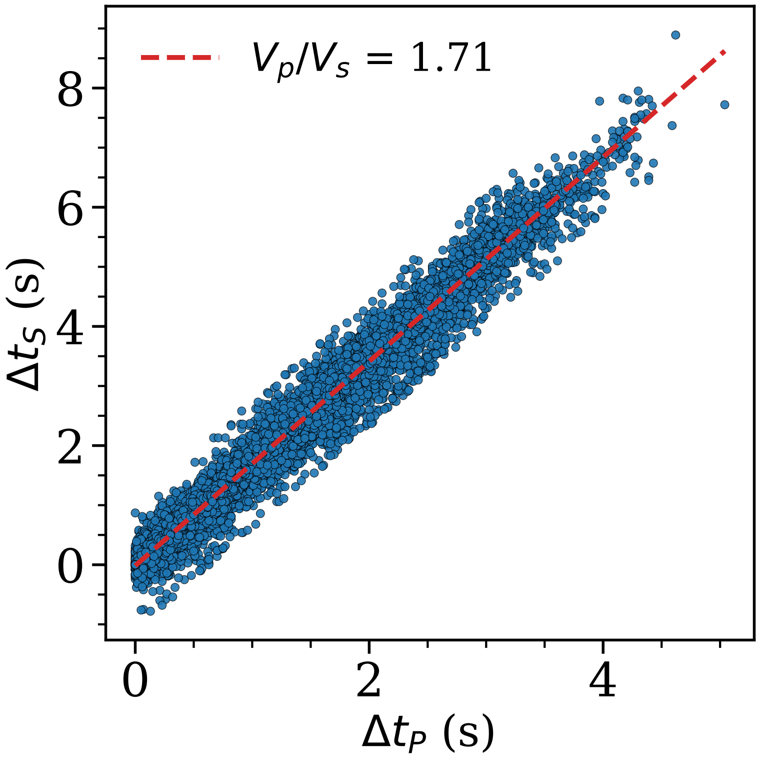

Figure S2. Relationship between the differential S- and P-wave travel times (Δt_S and Δt_P) for the earthquakes used to estimate the V_p/V_s ratio. The dashed red line represents the best-fitting linear regression, yielding $V_p/V_s \approx 1.71$.

and Δt_P) times measured at the same stations for the selected earthquakes. The slope of the best-fitting regression line yields a V_p/V_s ratio of approximately 1.71.

S1.2 RMS Residual Statistics of Velocity Inversions

To reduce dependence on the starting velocity model, synthetic velocity models were generated by perturbing the reference model of Srinagesh et al. (2020). Layer velocities were randomly perturbed within ±0.7 km s^{-1} and interface depths within ±2 km to produce 70 alternative starting models for each inversion stage. Each model was inverted independently using `VELEST` in simultaneous inversion mode. We adopted `INVERTRATIO = 2`, such that the velocity model was updated only every second iteration, while earthquake hypocenters and station corrections were updated during every iteration. This strategy allows the hypocenters and station delays to stabilize before subsequent velocity updates, thereby improving inversion stability and convergence. After the completion of each stage, consisting of 7 iterations, the final velocity model was obtained by computing the layer-by-layer mean of all successfully inverted velocity models. This averaged model was then used as the starting model for the next inversion stage and was again perturbed randomly to generate an ensemble of starting models. Three successive inversion stages were performed, resulting in a total of 210 inverted velocity models, from which the final mean velocity model was selected for use in all subsequent analyses.

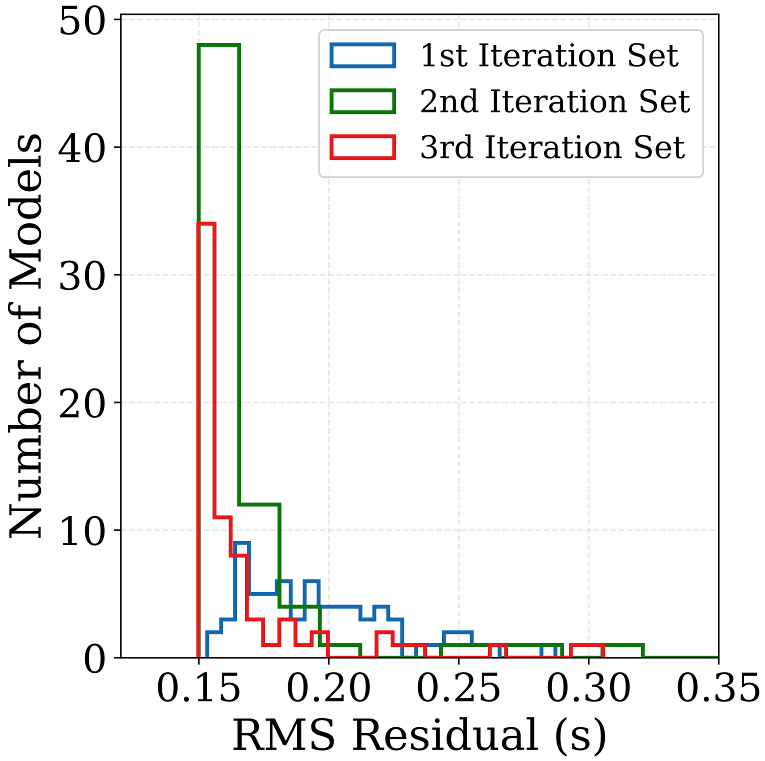

Figure S3. Distribution of RMS travel-time residuals obtained from velocity inversions during the three iteration stages of the inversion. The progressive reduction and convergence of RMS values indicate that the inversion approaches a stable velocity model.

Figure S3 shows the distribution of RMS travel-time residuals obtained from the inversions during the three iteration stages described in the main text. The first iteration set displays a broader range of RMS values reflecting the diversity of starting models. With subsequent inversion stages, the RMS residuals progressively decrease and converge toward a narrow range of values, indicating that the inversion approaches a stable minimum-misfit solution.

Using the final velocity model, earthquakes were relocated with `HypoInverse`. A comparison of location error ellipses before and after velocity inversion is shown in Figure S4, illustrating the reduction in location uncertainties achieved with the updated model.

Text S2. Earthquake detection, phase picking, and relocation

Earthquake detection and initial earthquake locations obtained using the BackProjection and Matched-Filtering (BPMF) workflow (Beaucé et al., 2024). Within the workflow, continuous three-component waveform data from the NGRI and NCS seismic networks were corrected for instrument response and band-pass filtered between 1 and 20 Hz. The original pretrained `PhaseNet` model (Zhu & Beroza, 2019) was applied to the continuous waveforms to generate continuous P- and S-wave probability time series, which were subsequently backprojected across the seismic network to identify coherent earthquake signals. Earthquake detections were identified using a backprojection threshold

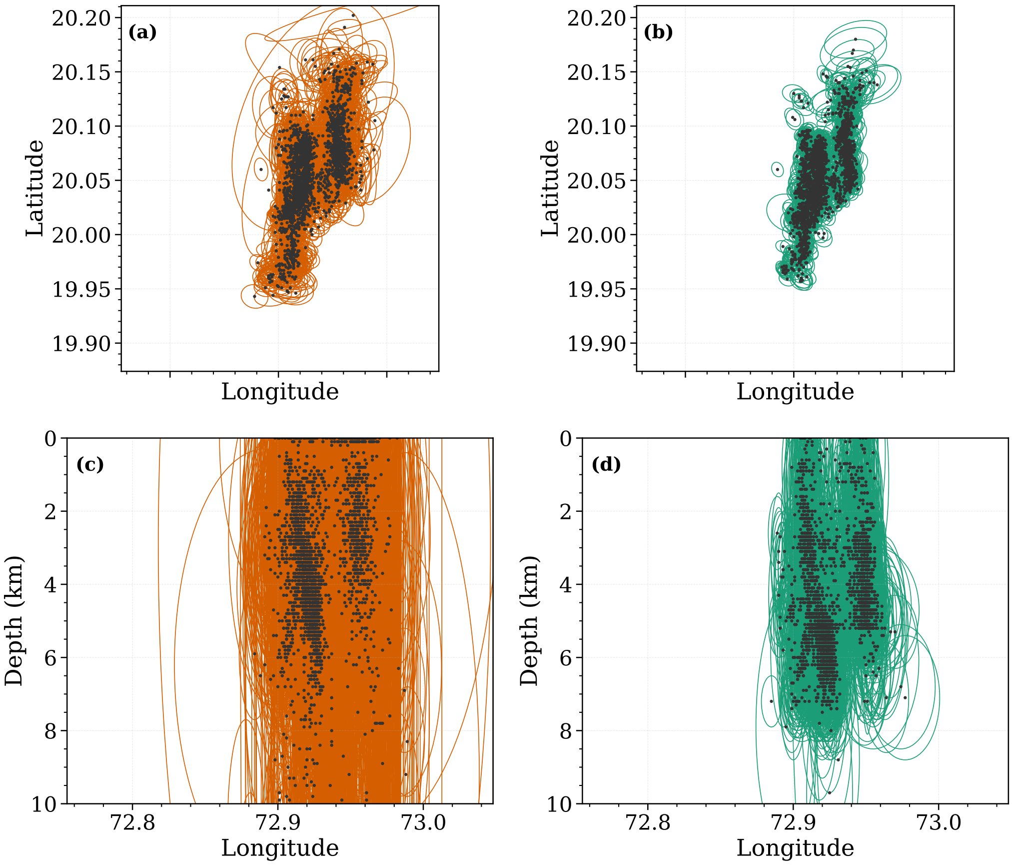

Figure S4. Comparison of earthquake location uncertainty ellipses before and after velocity inversion. Panels (a) and (c) show epicentral and depth–longitude distributions obtained using the initial velocity model, while panels (b) and (d) show results after relocation using the final velocity model derived in this study. Ellipses represent location uncertainties estimated from `HypoInverse`. The comparison illustrates the reduction in location uncertainty achieved using the updated velocity model.

of 2 (SI Figure S6), producing an initial machine-learning (ML) catalog of 57,826 detected events. The ML catalog recovered approximately 95% of the manually picked high-quality earthquakes (recorded by at least six stations) while substantially increasing the total number of detected events.

For each detected event, P- and S-wave arrival times were refined using `PhaseNet` in picking mode. The automatically determined phase arrivals were subsequently used as input to the probabilistic earthquake location program `NonLinLoc` (Lomax et al., 2000). Earthquake hypocenters were determined using the Equal Differential Time (EDT_OT_WT_ML) location algorithm, which combines differential travel-time residuals, weighted phase observations, and maximum-likelihood estimation to obtain robust hypocenter locations that are less sensitive to outlying phase picks. Only events with picks from at least six stations were considered for location, resulting in 20,638 well-located earthquakes. Approximately 88% of the manually picked earthquakes were successfully recovered after the initial location stage.

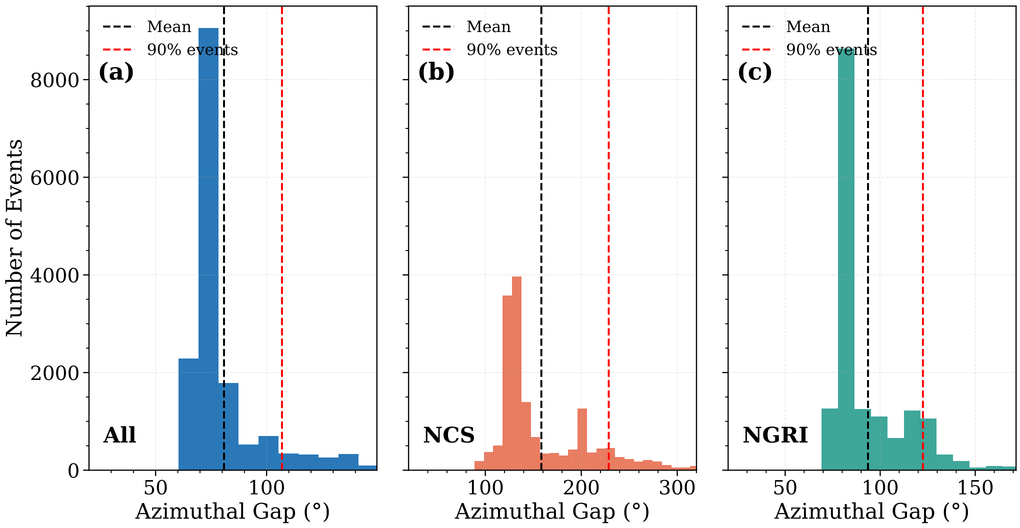

Figure S5. Distribution of azimuthal gap values for earthquake locations obtained using different seismic network configurations. (a) Azimuthal gap distribution for all relocated events used in this study. (b) Azimuthal gap distribution for locations determined using only the NCS network. (c) Azimuthal gap distribution for locations determined using only the NGRI network. Black dashed lines indicate the mean azimuthal gap for each dataset, while red dashed lines mark the azimuthal gap below which 90% of the events are located. The distributions show that most relocated events have azimuthal gaps below ∼107° for the full dataset, whereas the individual NCS and NGRI network solutions exhibit larger azimuthal gaps due to reduced station coverage.

Table 1. Seismic station information used in this study. Latitude and longitude are given in degrees, and elevation is given in meters above sea level.

Station	Latitude (°N)	Longitude (°E)	Elevation (m)
AINE	19.8940	72.8420	73
GAGO	19.9870	73.0280	101
KAIN	20.0240	72.7750	37
KAWA	20.1180	72.8790	51
MASA	20.1910	72.9430	44
UDHW	20.0940	73.0030	57
PALG	20.0350	72.9131	162
TLSR	20.1255	72.9133	57
SSNE	20.0275	72.9583	130
AMBR	20.0131	72.8583	70
DNVR	19.9775	72.9198	78

The `NonLinLoc` catalog was subsequently relocated using `GrowClust` (Trugman & Shearer, 2017), which refines relative earthquake locations by inverting differential travel times derived from waveform cross-correlation. Relative relocations were performed for event pairs with waveform cross-correlation coefficients of at least 0.8. This procedure yielded a final relocated catalog of 16,008 earthquakes, corresponding to approximately 81% of the manually picked catalog. The relocated catalog forms the basis for all spatiotemporal analyses presented in this study.

Uncertainties in earthquake locations were estimated using the GrowClust bootstrap procedure, in which hypocenter locations are perturbed, and the relocation is repeated to evaluate solution stability. Horizontal and vertical location uncertainties for events relocated with `GrowClust` are shown in Figure S7, which compares these uncertainties with those obtained from `NonLinLoc`, where location errors are derived from confidence regions of the posterior probability density function. The comparison highlights the improved relative location precision achieved using the cross-correlation-based relocation approach.

Text S3. Moment tensor solutions

This section provides additional details of the moment tensor inversion procedure summarized in the main text. Moment tensor inversions were performed using `MTTime` (Ichinose et al., 2014), with displacement Green's functions computed using the Computer Programs in Seismology (CPS) package (Herrmann, 2013) for the final one-dimensional velocity model derived in this study. Instrument responses were removed prior to processing, and the three-component broadband waveforms were converted to displacement and band-pass filtered between 0.05 and 1 Hz using a two-pole Butterworth filter. For each station, waveform windows were extracted around the P-wave arrival, extending from 2 s before the arrival to 6–8 s after the arrival, with the post-arrival window length adjusted according to the source–receiver distance.

Inversion quality was evaluated using the variance reduction (VR) between the observed and synthetic waveforms across all available stations. Only solutions with VR exceeding 50% were retained. Table 2 summarizes the source parameters, nodal-plane geometry, moment tensor decomposition, and inversion quality metrics for the 37 accepted events, while Figure S8 shows the spatial distribution of the corresponding deviatoric moment tensor solutions for the same set of earthquakes from Figure 3.

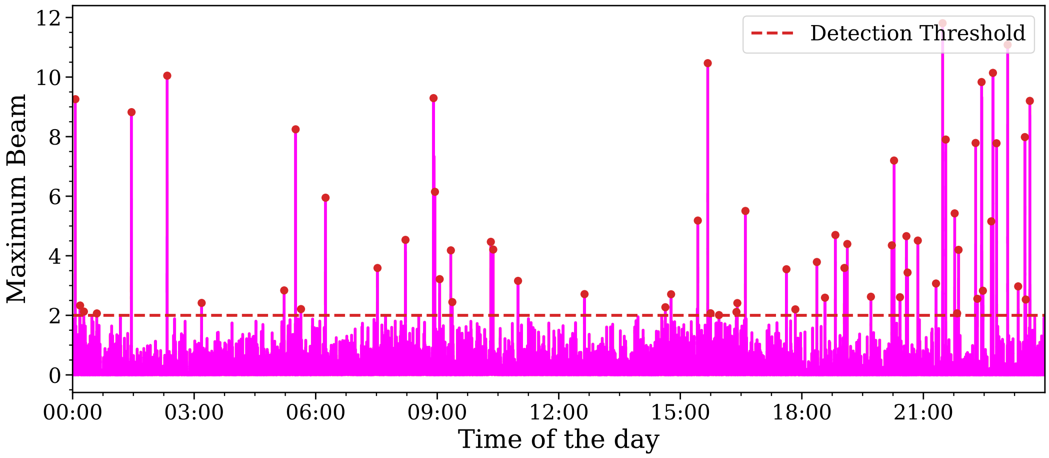

Figure S6. Example of the maximum beam power time series computed across the seismic network for a single day during the swarm sequence. The red dashed line marks the detection threshold (beam power = 2), and peaks exceeding this threshold were identified as candidate earthquakes. A total of 63 detections were identified for the day shown.

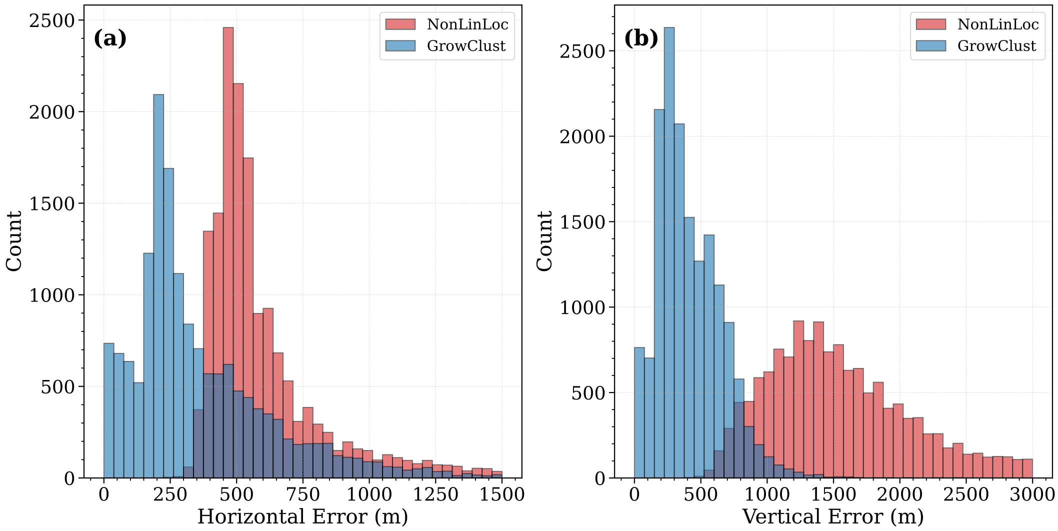

Figure S7. Comparison of earthquake location uncertainties obtained from `NonLinLoc` and `GrowClust`, showing (a) horizontal and (b) depth uncertainties.

The distributions of strike, dip, and rake angles are summarized in Figure S9. The strike orientations define two dominant north–south trending populations that closely match the relocated seismicity clusters and support the interpretation of two subparallel fault strands. Dip angles cluster around $\sim$ 30° and $\sim$ 60°, consistent with conjugate normal faults, whereas rake angles are concentrated near 270°, indicating predominantly normal faulting with only minor strike-slip components.

Representative waveform fits are shown in Figure S10. The examples correspond to the accepted solutions with the highest (65%) and lowest (50%) variance reductions. In both cases, the synthetic waveforms reproduce the observed radial, transverse, and vertical components well over the adopted frequency band, demonstrating that the inferred source mechanisms are robust across the range of accepted inversion qualities.

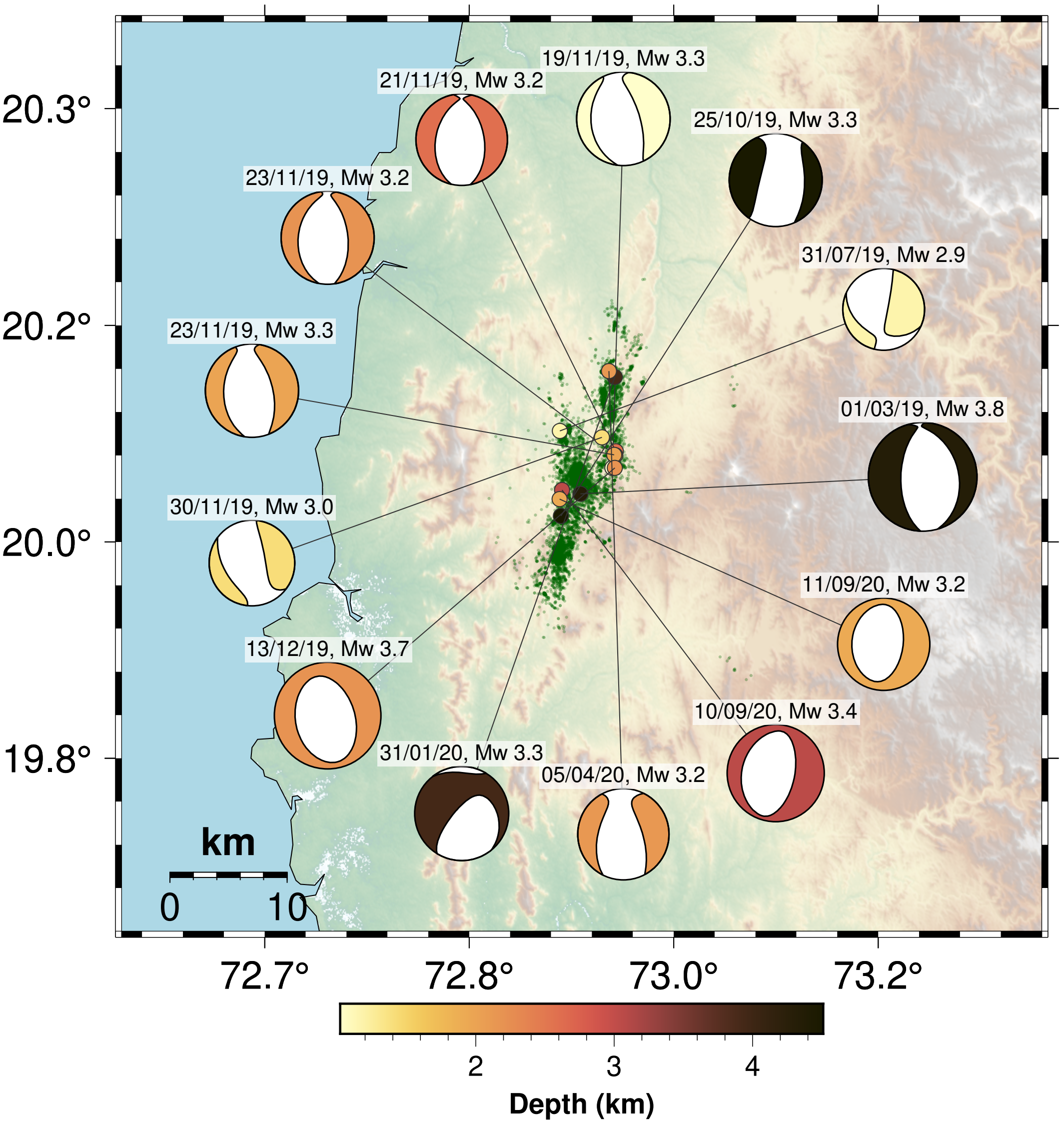

Figure S8. Deviatoric moment tensor solutions for the same set of earthquakes from Figure 3. Beachball symbols represent full deviatoric solutions (double-couple + CLVD) plotted at relocated epicenters and color-coded by depth.

Text S4. Influence of Catalog Resolution on Inferred Swarm Migration

The migration behavior inferred from the Palghar swarm depends strongly on the accuracy and density of the earthquake catalog. SI Figure S11 compares the distance–time evolution obtained from the initial human-picked catalog containing 10,377 events with the migration envelopes derived from the relocated catalog used in this study. Although the initial catalog captures the broad temporal expansion of the swarm, the substantial scatter in earthquake locations obscures the detailed migration fronts and makes it difficult to distinguish the different phases of swarm evolution. In particular, the delayed activation of the eastern fault, the rapid migration episodes, and the temporal evolution of the leading seismicity fronts are not clearly resolved.

Table 2. Moment tensor solutions for earthquakes with $M_l > 3.0$ and variance reduction exceeding 50%. The table lists the event origin time (Event ID), hypocentral location, magnitude, and the strike, dip, and rake parameters of the two nodal planes obtained from the moment tensor inversion. The percentage contributions of the double-couple (DC) and compensated linear vector dipole (CLVD) components of the deviatoric moment tensor solution are also reported.

Event ID	Lat (°N)	Lon (°E)	Depth (km)	Fault Plane 1 (S/D/R)	Fault Plane 2 (S/D/R)	DC/CLVD/ISO (%)	VR (%)	M_w
2019_03_01_05_44_25	20.037	72.924	4.83	345/36/−103	181/55/−81	97/3/0	58.2	3.79
2019_03_10_08_25_26	20.054	72.908	1.64	1/57/−96	192/33/−81	98/2/0	52.9	2.74
2019_03_10_19_30_10	20.051	72.920	5.12	206/65/−67	341/34/−130	85/15/0	55.7	3.17
2019_03_10_22_21_49	20.055	72.908	1.56	335/58/−119	201/42/−52	68/32/0	51.3	2.76
2019_03_31_12_21_57	20.049	72.923	5.58	40/72/−73	176/25/−132	95/5/0	57.1	3.09
2019_05_13_06_31_26	20.046	72.921	6.32	180/31/−115	28/62/−76	84/16/0	59.0	2.99
2019_07_24_19_48_28	20.056	72.909	1.51	181/35/−90	1/55/−90	85/15/0	67.8	2.75
2019_07_31_14_50_03	20.085	72.907	1.18	113/37/−167	13/82/−54	93/7/0	59.2	2.86
2019_10_24_19_12_15	20.063	72.950	1.85	5/54/−84	175/37/−98	83/17/0	59.5	2.79
2019_10_25_22_35_41	20.020	72.908	4.51	201/60/−71	346/36/−120	50/50/0	59.8	3.27
2019_11_19_20_05_44	20.057	72.950	1.02	342/61/−99	180/30/−74	89/11/0	55.1	3.27
2019_11_19_20_26_47	20.059	72.949	0.82	173/32/−89	351/58/−91	94/6/0	55.1	2.79
2019_11_19_20_57_41	20.052	72.952	0.78	351/64/−95	183/26/−79	80/20/0	50.2	2.66
2019_11_21_01_50_28	20.070	72.953	2.60	193/43/−73	350/49/−106	100/0/0	50.2	3.19
2019_11_23_15_10_48	20.067	72.952	2.20	189/37/−78	354/54/−99	98/2/0	60.9	3.25
2019_11_23_20_31_13	20.067	72.951	1.99	344/53/−102	184/39/−74	91/9/0	60.2	3.26
2019_11_24_12_12_25	20.044	72.940	1.58	178/27/−82	349/63/−94	96/4/0	51.1	2.70
2019_11_25_21_15_55	20.039	72.945	1.58	178/27/−82	349/63/−94	96/4/0	51.1	2.70
2019_11_27_01_25_37	20.047	72.952	1.52	2/58/−95	190/32/−83	89/11/0	61.0	2.71
2019_11_30_11_41_33	20.081	72.941	1.42	358/62/−64	131/37/−130	62/38/0	54.6	3.01
2019_12_03_06_09_23	20.093	72.944	1.57	5/59/−78	164/33/−108	92/8/0	55.4	2.65
2019_12_03_22_17_43	19.964	72.889	1.87	13/58/−93	199/33/−85	87/13/0	50.1	2.66
2019_12_13_23_52_38	20.057	72.952	1.70	341/53/−105	185/40/−71	95/5/0	56.9	3.68
2019_12_14_09_05_05	20.101	72.950	1.24	9/59/−72	157/35/−117	97/3/0	52.1	2.70
2019_12_14_10_47_34	20.063	72.951	1.55	179/38/−94	4/52/−87	79/21/0	63.1	2.77
2019_12_15_00_31_28	20.015	72.920	2.91	202/65/−78	356/27/−114	94/6/0	55.7	3.03
2019_12_15_03_49_17	20.002	72.908	3.02	343/42/−144	225/67/−54	88/12/0	61.4	2.79
2019_12_15_19_27_56	20.049	72.922	4.63	181/89/98	277/8/6	96/4/0	59.2	2.82
2020_01_31_07_54_42	20.127	72.952	3.93	217/80/−61	324/30/−160	76/24/0	53.0	3.30
2020_02_23_04_43_02	20.067	72.952	1.92	177/43/−89	355/47/−91	95/5/0	53.2	2.73
2020_03_19_03_49_08	20.048	72.923	5.87	15/68/−66	144/32/−136	91/9/0	52.1	3.09
2020_04_01_18_09_18	20.044	72.921	6.29	165/31/−125	25/65/−71	92/8/0	55.5	3.01
2020_04_05_18_48_30	20.131	72.947	2.63	210/44/−46	337/60/−124	79/21/0	50.3	3.21
2020_09_10_22_27_48	20.040	72.909	3.06	11/58/−93	196/32/−85	91/9/0	53.6	3.39
2020_09_11_01_36_02	20.033	72.907	1.92	7/57/−88	184/33/−93	80/20/0	65.7	3.23
2020_09_21_21_20_44	20.050	72.922	2.87	201/34/−72	359/57/−102	86/14/0	58.5	2.90
2020_09_22_19_11_15	20.038	72.904	1.79	19/62/−90	200/28/−89	64/36/0	51.0	2.78

Application of `NonLinLoc` to the densified ML-enhanced catalog improves the overall spatial coherence of the seismicity and captures the first-order expansion of the swarm (SI Figure S12). The eastern, western, and off-fault seismicity clusters become more readily distinguishable, and the broad diffusive character of the swarm is preserved. However, the location precision remains insufficient to clearly resolve the fault-scale migration fronts, persistent seismicity bands, and episodic along-strike and along-dip migration patterns revealed by the subsequent `GrowClust` relocations.

The `GrowClust` relocations further sharpen the seismicity distribution and reveal the detailed spatiotemporal patterns analyzed in the main text. The improved relative locations delineate persistent localized seismicity along the western fault, distinct migration episodes along both fault systems, and the close correspondence between on-fault and off-fault migration patterns. These comparisons demonstrate that the combination of catalog densification and high-precision relative relocation is essential for understanding the processes governing the evolution of the Palghar swarm.

Text S5. Along-Strike, Along-Dip, and Off-Fault Migration Patterns of the High-Resolution Relocated Seismicity

To further investigate the migration behavior of the Palghar swarm, we analyzed the temporal evolution of seismicity projected along the strike and dip directions of the western and eastern faults. Earthquake locations were projected onto fault-parallel co-

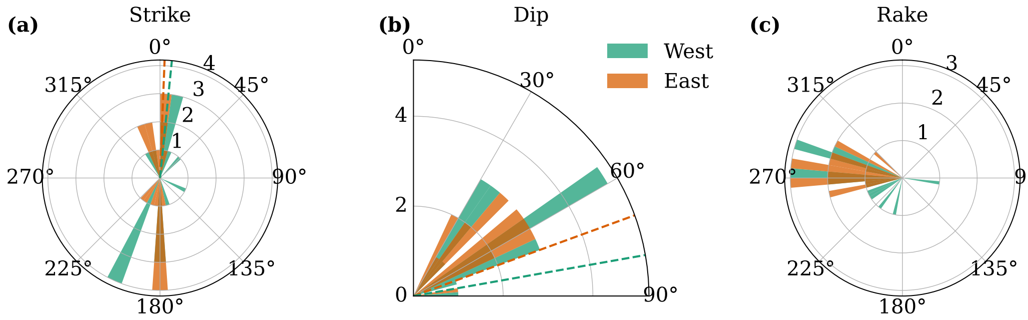

Figure S9. Rose diagrams showing the distribution of focal mechanism parameters derived from moment tensor solutions for 37 earthquakes with local magnitude ($M_l > 3.0$) in the Palghar swarm sequence. (a) Distribution of strike angles for the western (green) and eastern (orange) fault systems. The strike distributions consistent with the mapped geometry of the fault network. (b) Distribution of dip angles for both fault systems. Dashed lines indicate the mean dip orientation of the western and eastern fault planes inferred from relocated seismicity. Most events exhibit moderately to steeply dipping fault planes. (c) Distribution of rake angles for the two fault systems. The rake distributions are strongly clustered near$\sim$ 270°, indicating predominantly normal faulting with a minor strike-slip component.

ordinate systems, and the evolution of the migrating seismicity fronts was tracked using the 95th and 5th percentile envelopes of seismicity through time.

For the western fault, seismicity remains strongly concentrated within persistent central bands located near ∼1.2 km in the along-dip direction and ∼1.6 km in the along-strike direction. To better resolve the migration of the seismicity fronts, events within these highly populated bands were excluded from the percentile calculations using windows of ±0.5 km and ±0.7 km in the along-dip and along-strike projections, respectively. The resulting distance-time evolution reveals strongly episodic migration, characterized by multiple propagating fronts, abrupt reversals, and back-propagating seismicity streaks along both strike and dip directions. A prominent down-dip migration episode is observed between approximately 260 and 460 days (migration 6 in SI Figure S13a), followed by a later phase of up-dip and southward migration between approximately 480 and 640 days (migrations 8 and 12 in SI Figure S13a,c). Several additional shorter-duration migration episodes occur throughout the sequence, indicating repeated reorganization of seismicity along the fault.

In contrast, the eastern fault exhibits a more spatially localized migration pattern. Following its activation at approximately 260 days, seismicity remains concentrated near the central portion of the fault before progressively expanding along the dip direction. After approximately 400 days, the seismicity envelope broadens, with expansion toward updip and a pronounced down-dip migration of the lower migration front during the later stages of the sequence (migration 2 in SI Figure S14a). In the along-strike projection, the leading migration front propagates northward between approximately 260 and 460 days (migrations 3 and 4 in SI Figure S14c). At the same time, a weaker migration front develops toward negative along-strike distances (migration 5).

To further examine the relationship between on-fault and off-fault seismicity, we compared the epicentral migration of the off-fault events with that of the eastern fault (SI Figure S15 a, d). Between approximately 260 and 460 days, both clusters exhibit nearly identical migration rates. During the initial stage of this interval (approximately 260–360 days), the off-fault seismicity also reproduces the northward migration pattern observed along the eastern fault (SI Figure S15 b, c). This correspondence becomes even more apparent when the on-fault clusters are restricted to narrower bands of ±500 m around the interpreted fault traces (SI Figure S15 e, f), demonstrating that the observed migration patterns are robust and insensitive to the choice of fault-zone width. During the later stages of the sequence (approximately 480–640 days), the southward and updip migration observed along the western fault is similarly mirrored by adjacent off-fault seismicity immediately west of the fault (SI Figure S16). These observations demonstrate that the off-fault seismicity closely tracks the migration of the active fault systems throughout the evolution of the swarm.

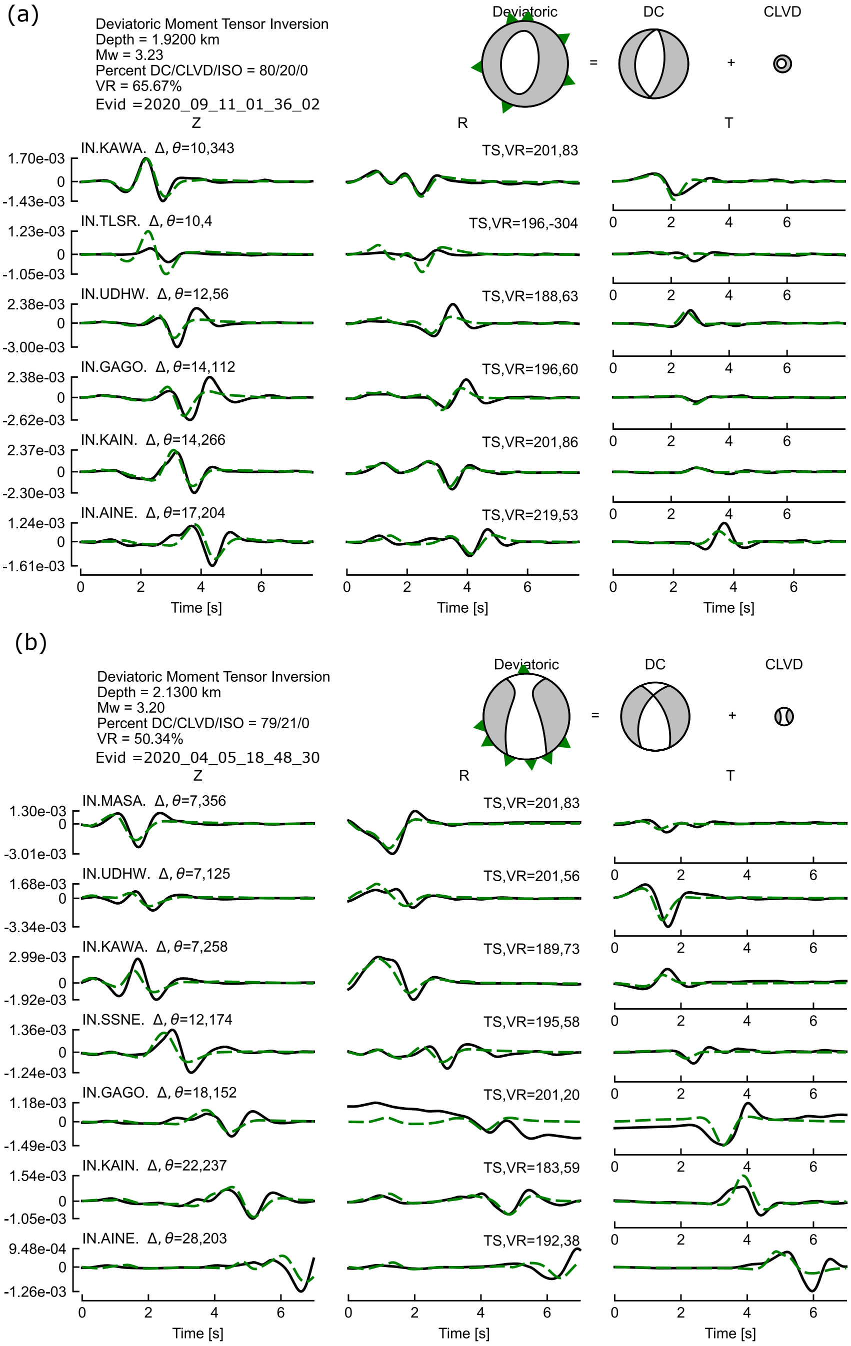

Figure S10. Deviatoric moment tensor inversion results for two Palghar earthquakes filtered between 0.05–1 Hz. (a) Event on 2020-09-11 (M_w 3.23) with the highest variance reduction (VR = 65%). (b) Event on 2020-04-05 (M_w 3.21) with the lowest variance reduction (VR = 50%). Black lines are observed waveforms, green lines are synthetics, shown for radial (R), transverse (T), and vertical (Z) components. Beachball diagrams show deviatoric solutions, with percentage decomposition and overall VR listed above each event.

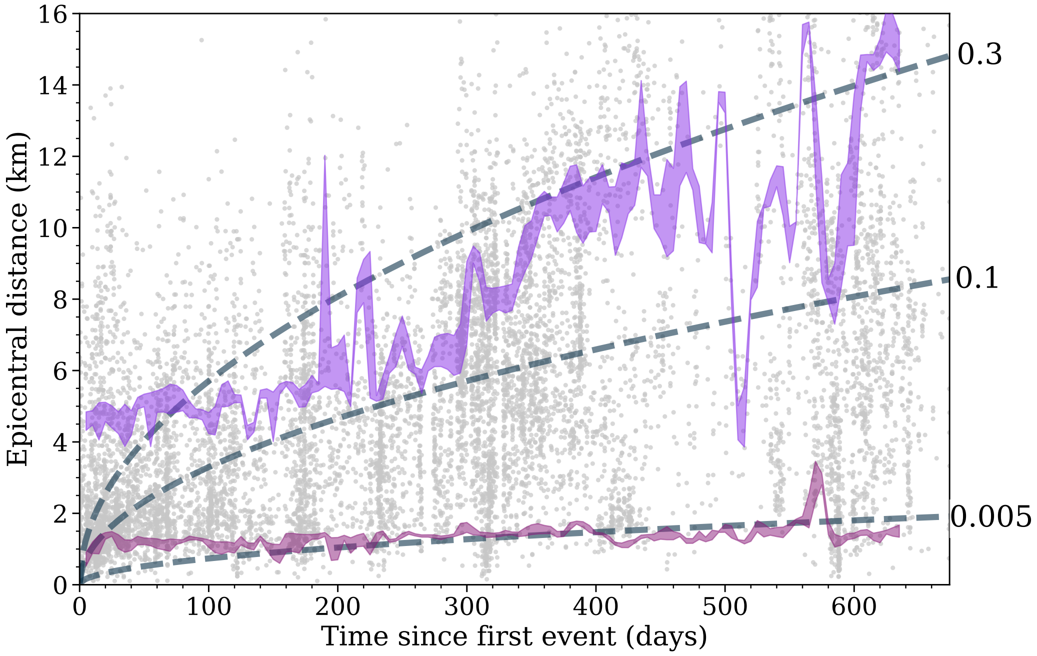

Figure S11. Epicentral distance as a function of time since the first detected event for the 10,377 earthquakes in the initial human-picked catalog (gray dots). Dashed curves indicate theoretical diffusion fronts corresponding to apparent diffusivities of $D = 0.005$, 0.1, and 0.3 m^2 s^{-1}. The purple and pink shaded regions show the 95th and 5th percentile migration envelopes obtained from the relocated catalog, with shaded bounds denoting the associated ±2.5% percentile range. The figure illustrates that the diffuse nature of the initial earthquake locations obscures the detailed migration fronts and spatiotemporal patterns that become evident only after relocation.

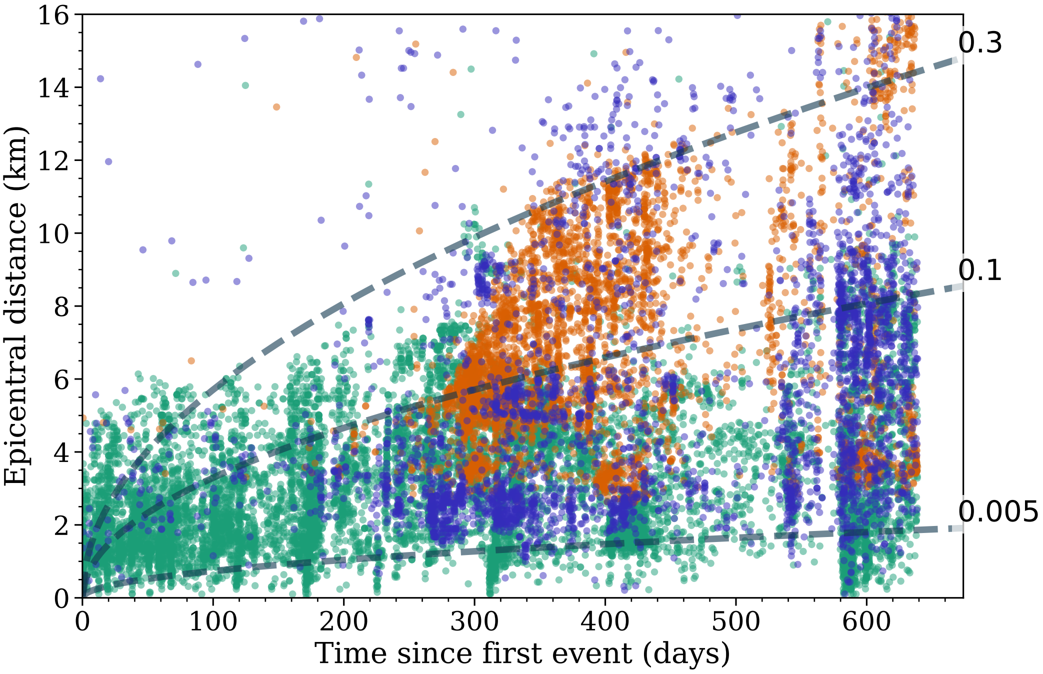

Figure S12. Distance–time evolution of the Palghar swarm using 20,638 earthquakes located with `NonLinLoc` and recorded by six or more stations. Green, orange, and blue dots represent earthquakes associated with the western cluster, eastern cluster, and off-fault seismicity, respectively. Epicentral distance from the first detected event is plotted as a function of time since swarm initiation. Dashed curves represent reference diffusion fronts corresponding to apparent diffusivities of 0.005, 0.1, and 0.3 m^2 s^{-1}. The figure illustrates the broad spatiotemporal expansion of the swarm resolved by the `NonLinLoc` locations and serves as a reference for comparison with the higher-resolution catalog obtained from `GrowClust` relocations using waveform cross-correlation coefficients ≥ 0.8.

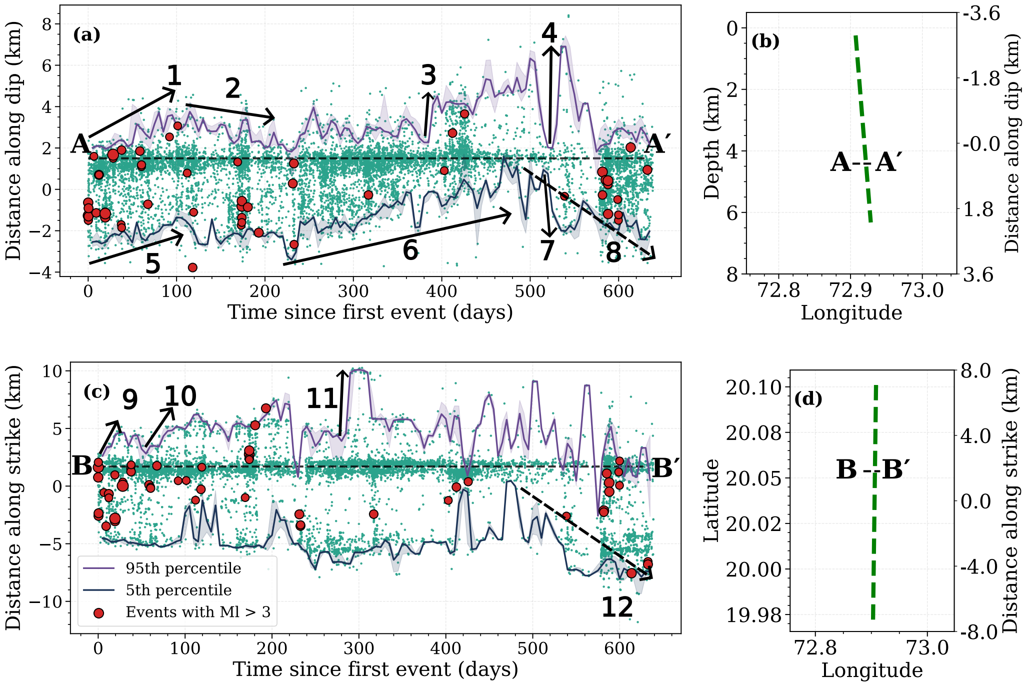

Figure S13. Spatiotemporal evolution of seismicity migration along the western fault. (a,c) Earthquake locations are projected onto along-dip and along-strike profiles as a function of time since the first detected event. Green dots represent relocated earthquakes and red circles denote events with $M_l > 3$. Purple and dark-blue curves show the 95th and 5th percentile positions of seismicity, respectively. The arrows and numbered labels identify major migration episodes. (b,d) Geometry of the projection profiles used for calculating along-dip and along-strike migration distances.

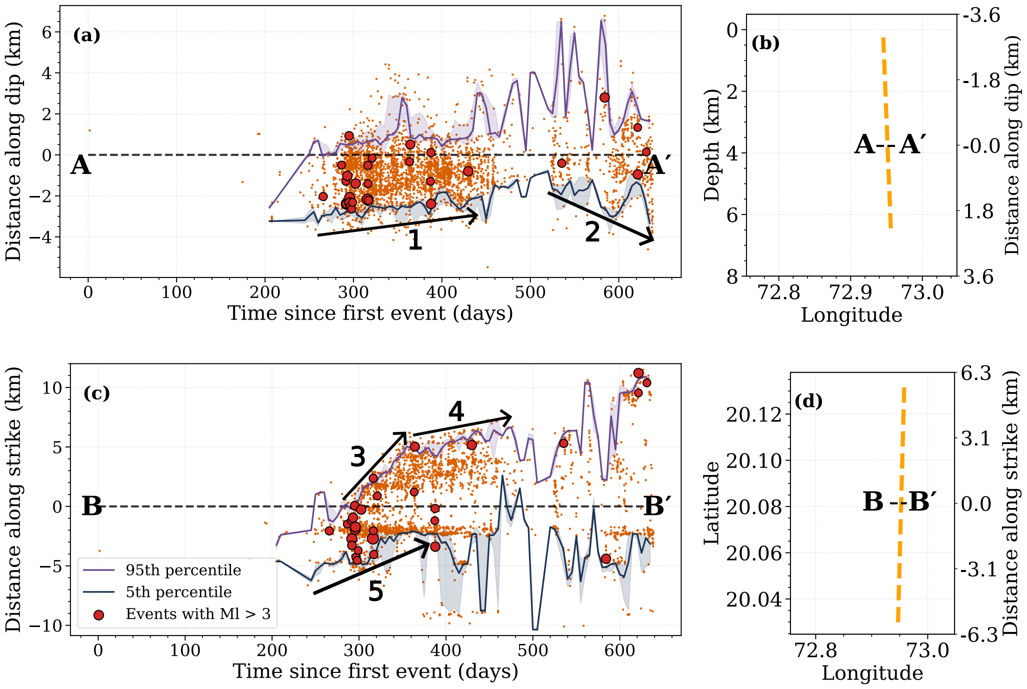

Figure S14. Spatiotemporal evolution of seismicity migration along the eastern fault. (a,c) Earthquake locations are projected onto along-dip and along-strike profiles as a function of time since the first detected event. Orange dots represent relocated earthquakes, and red circles denote events with $M_l > 3$. Purple and dark-blue curves show the 95th and 5th percentile positions of seismicity, respectively, highlighting the evolution of the migrating seismicity fronts. Arrows indicate the dominant migration direction along strike. (b,d) Geometry of the projection profiles used for calculating along-dip and along-strike migration distances.

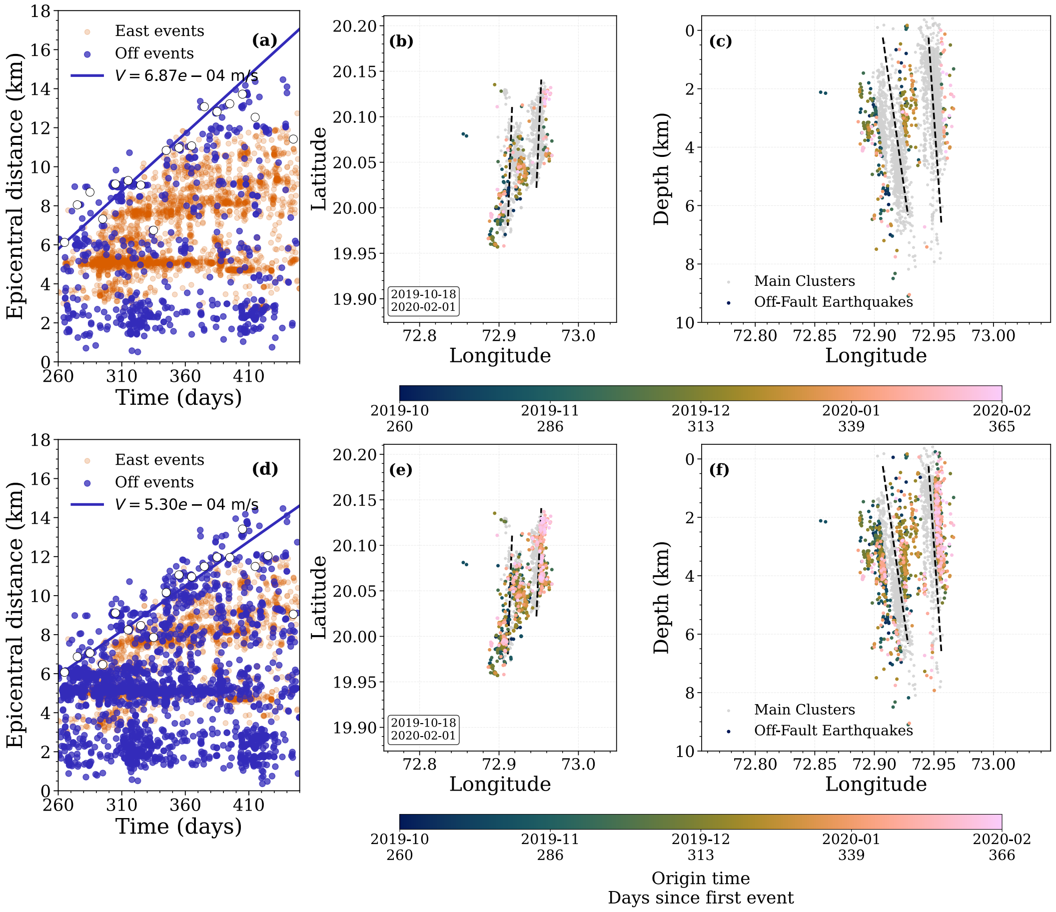

Figure S15. Migration of off-fault seismicity associated with the rapid migration episode on the eastern fault (migration 3 in Figure S14). (a) Epicentral distance as a function of time for off-fault earthquakes identified using a ±1 km fault-zone definition. Orange and blue dots represent eastern-fault and off-fault earthquakes, respectively. The solid blue line shows a linear fit to the leading migration front of the off-fault seismicity, corresponding to a migration velocity of 6.87×10^{-4} m s^{-1}. (b) Map-view and (c) longitude–depth projections of the seismicity during the 260–360 day interval. Gray dots represent on-fault earthquakes associated with the eastern and western fault systems, while colored dots denote off-fault earthquakes color-coded by origin time. The off-fault seismicity exhibits the same northward migration pattern observed along the eastern fault (migration 3 in SI Figure S14). (d–f) Same as (a–c), but using a stricter on-fault definition in which earthquakes within ±500 m of the interpreted eastern and western fault planes are classified as on-fault events, with all remaining earthquakes assigned to the off-fault population. The estimated off-fault migration velocity (5.30×10^{-4} m s^{-1}) and the spatiotemporal migration pattern remain largely unchanged, indicating that the observed off-fault migration is robust and not sensitive to the fault-zone width used to classify earthquakes.

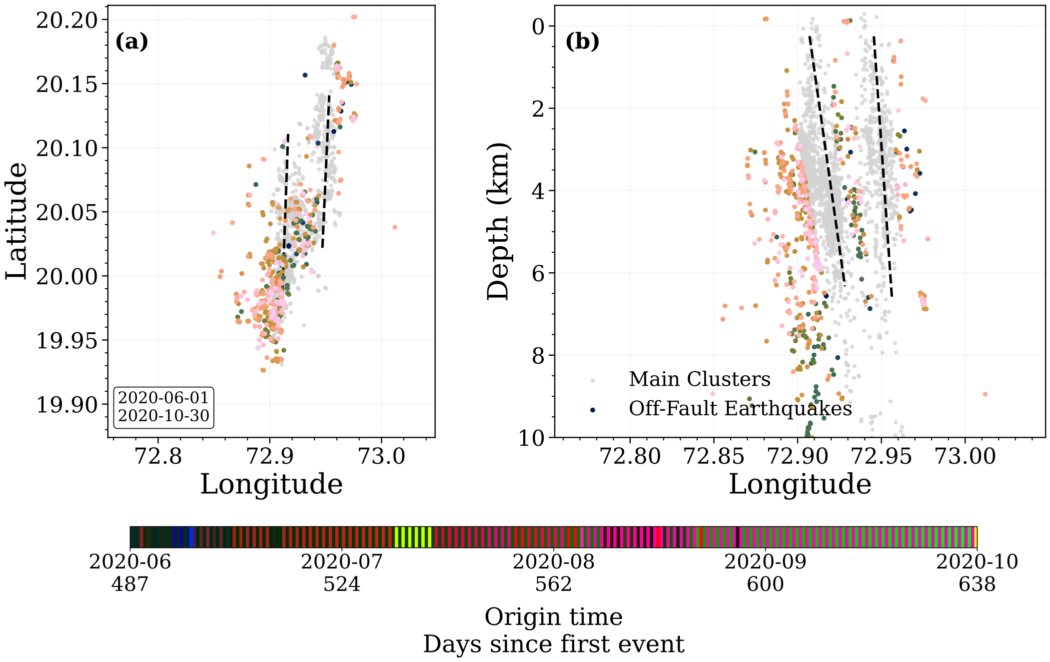

Figure S16. Spatiotemporal evolution of off-fault seismicity during the late stages of the Palghar swarm sequence (2020-06-01 to 2020-10-30, 480 to 640 days). Gray dots represent earthquakes associated with the western and eastern faults, while colored dots denote off-fault earthquakes, color-coded by origin time. (a) Map view and (b) longitude–depth projection of the off-fault seismicity. Dashed gray lines indicate the approximate geometry of the western and eastern fault planes inferred from relocated seismicity. The off-fault earthquakes exhibit migration patterns that closely mirror contemporaneous migration along the main fault systems, including the up-dip expansion observed on both the western and eastern faults and the southward migration episode identified on the western fault. These migrations correspond to episodes 8 and 12 on the western fault and episode 2 on the eastern fault (see SI Figures S13 and S14), highlighting the close spatiotemporal relationship between on-fault and off-fault seismicity.

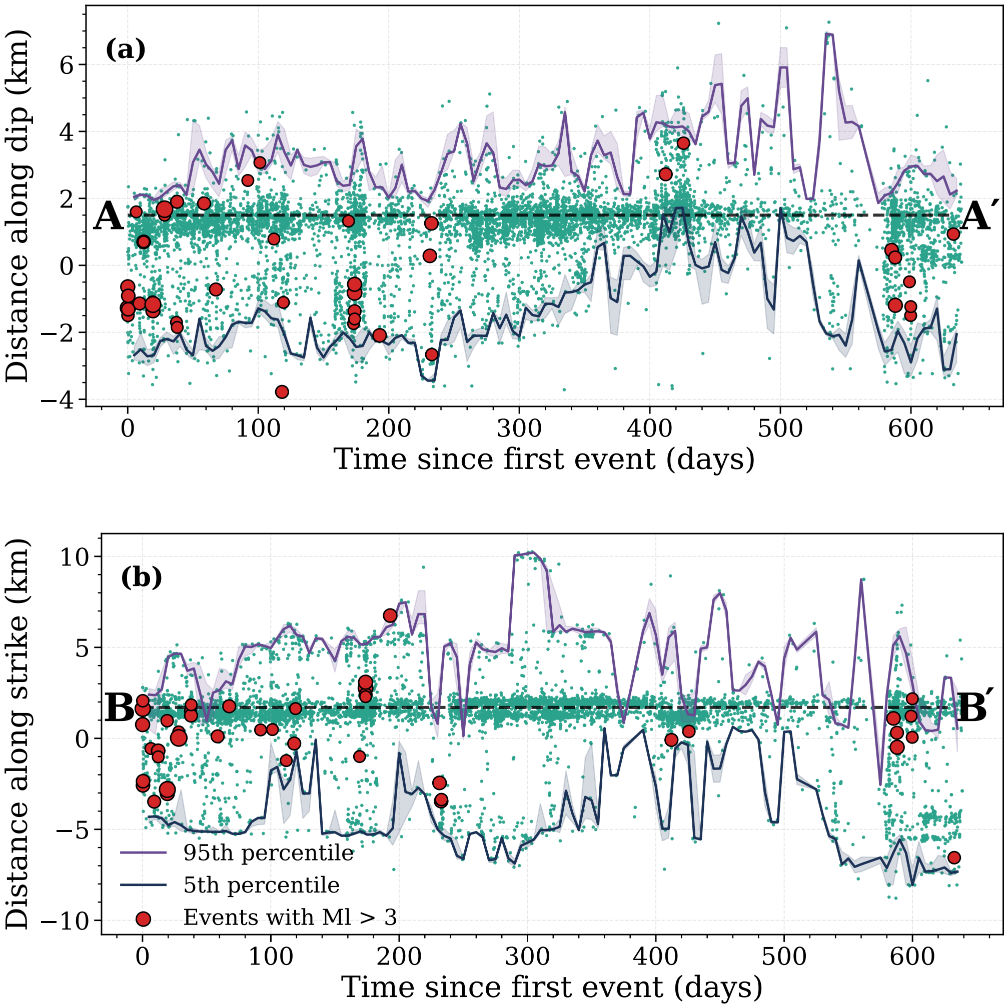

Figure S17. Spatiotemporal evolution of seismicity along the western fault after restricting the fault-zone width to ±500 m around the interpreted fault plane. Earthquakes are projected onto the along-dip (a) and along-strike (b) directions as a function of time since the first detected event. Green dots represent relocated earthquakes, while red circles denote larger events with local magnitude ($M_l > 3$). The horizontal dashed lines mark the dominant seismicity band. Purple and dark-blue curves show the 95th and 5th percentile positions of seismicity, respectively, with shaded regions indicating the associated ±2.5% percentile bounds. Despite the substantially narrower fault-zone definition, a persistent and spatially confined seismicity band remains evident in both the along-dip and along-strike projections throughout most of the swarm evolution, demonstrating that the long-lived seismicity concentration along the western fault is a robust feature and not an artifact of the fault-zone width used for event classification.

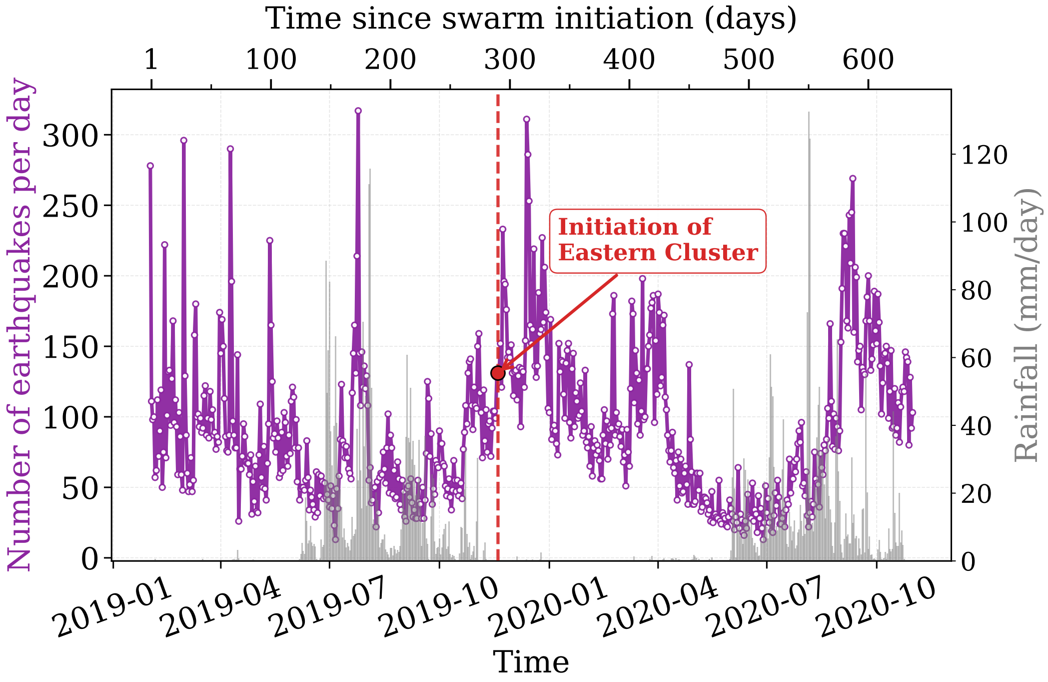

Figure S18. Time evolution of daily earthquake frequency during the Palghar swarm sequence from February 2019 to October 2020, comprising a total of 57,826 earthquakes detected in the ML-based earthquake catalog developed in this study. The purple curve shows the number of earthquakes per day, while gray bars represent daily rainfall. The red dashed line marks the onset of seismicity on the eastern fault. The periods of highest seismicity rates occur during the early stages of the sequence and do not show an obvious correspondence with seasonal rainfall variations. Daily precipitation data were obtained from the NASA Langley Research Center Prediction Of Worldwide Energy Resources (POWER) Project Daily API.